UNIVERSITAT DE BARCELONA

Facultat de Física

Departament d'Electrònica

Metal Additive Distribution in TiO_2 and SnO_2 Semiconductor Gas Sensor Nanostructured Materials

Jordi Arbiol i Cobos

Directors:

Dr. Albert Cornet i Calveras i Dra. Francesca Peiró Martínez

Memòria presentada per optar al grau de

Doctor en Ciències Físiques

Programa de Doctorat: Enginyeria i Materials Electrònics i Òptica

Tutor: Dr. Albert Cornet i Calveras

Bienni: 1997-99

Barcelona, 19 de juliol de 2001

Albert Cornet i Calveras, Catedràtic del Departament d'Electrònica de la Facultat de Física de la Universitat de Barcelona, com a Director i Tutor,

i

Francesca Peiró Martínez, Professora Titular del Departament d'Electrònica de la Facultat de Física de la Universitat de Barcelona, com a Directora,

CERTIFIQUEN:

Que la memòria "**Metal Additive Distribution in TiO_2 and SnO_2 Semiconductor Gas Sensor Nanostructured Materials**", que presenta en Jordi Arbiol i Cobos per optar al grau de Doctor en Ciències Físiques, s'ha realitzat sota la seva direcció.

Barcelona, 19 de Juny de 2001

Prof. Dr. Albert Cornet i Calveras Dra. Francesca Peiró Martínez

Per tu, Mirjana

Per vosaltres, Pares

En record a vosaltres, Pere i Emilio,
Avis estimats

Contents

Preface and Outline

Recently, there has been an increasing interest in the electronics world for those aspects related to semiconducting gas sensor (SGS) materials. In view of the increasingly strict legal limits for pollutant gas emissions, there is a great interest in developing high performance gas sensors for applications such as controlling air pollution and exhaust gases. In this way, semiconductor gas sensors offer good advantages with respect to other gas sensor devices (such as spectroscopic and optic systems), due to their simple implementation, low cost and good reliability for real-time control systems.

In the last few years, the Department of Electronics of the Universitat de Barcelona has been focussing part of the efforts to this field of knowledge, obtaining great results in the synthesis and characterization of semiconductor gas sensing materials, as well as in the development and test of gas sensor devices. Nevertheless, the comprehension of the main physical

and chemical phenomena that undergoes at sensing material are still a weak point under study. In order to improve the comprehension of the sensing phenomena more studies are needed, especially those related with surface physics and chemistry and the nanocrystalline properties of the sensing materials.

Although there exist many works in literature devoted to the electrical and general analytical characterization as well as to the understanding of the physical mechanisms that rule the gas sensing behavior, just few works have been dedicated to the nanostructural characterization of semiconductor nanopowders and metal additives morphology and distribution in this SGS systems. Attending to these considerations, we wanted to implement and develop in our department those nanoscopical techniques that allowed the further studies needed in SGS materials field. The enrich collaborations with Departamento de Ciencia de los Materiales e Ingeniería Metalúrgica y Química Inorgánica of the Universidad de Cádiz and with the Centre d'Elaboration de Matériaux et d'Etudes Structurales, CEMES-CNRS, of Toulouse have been of great importance in order to improve the knowledge about nanostructural characterization. The work performed in TEM and HRTEM related techniques have given us a good understanding of the nanoscopic characteristics and behavior of our materials. The latest results obtained in this field are summarized in this Ph.D. thesis work.

In the present work, we have been especially interested in the study of the different ways of metal additive distribution in the most common SGS materials used nowadays and furthermore in the physical and chemical sensing properties they can achieve. This *thesis* has been organized as follows:

Chapter 1 has been divided in two main parts, in the first one, we have given a general brief approach to semiconductor gas sensors especially focussing our efforts in the description of the general characteristics of the materials used in this work. A basic description of the sensing mechanisms involved in gas detection has been also given. In a second part, we have

introduced the most common ways of metal additive disposition in semiconductor nanopowders, such as: *Metal Diffusion* inside semiconductors bulk, *Superficial Clustering*, *Metal Macro-Agglomeration* and *Metal Ultradispersion*. So the background presented in this *Chapter* will be of great interest in order to understand and follow the results and discussions established in the following *Chapters*.

Chapter 2 has been devoted to give a brief review of the commonly used techniques for SGS nanopowders characterization. In a first part, we have presented an overview of those spectroscopic techniques such as X-Ray Diffraction, X-ray Photoelectron Spectroscopy, Raman Spectroscopy and Induced Coupled Plasma, which can promote a good general characterization about chemical and phase composition of the samples. In the second part, we have extended on the description of those TEM related techniques, such as conventional Transmission Electron Microscopy, High Resolution TEM, Selected Area Electron Diffraction and Electron Dispersive X-Ray Spectroscopy, which are intended to be a powerful tool in order to provide a nanostructural characterization of the SGS materials. The Digital Image Processing and Computer Image Simulation have been also presented as indispensable complementary tools to HRTEM as we will also see in the next *Chapters*, when applying these techniques to the analysis of the different types of metal distribution.

In *Chapter 3*, we have taken the Nb/TiO_2 systems since, as we have seen, the Nb can enter substitutionally inside TiO_2 structure, in the place of Ti vacancies. This *Chapter* has been devoted to the study of the influence of the *Metal Diffusion* inside the semiconductors nanopowders bulk. In this way, we have presented a complete study of the influence of Niobium loading percentage in the anatase to rutile phase transition. This part has been achieved by spectroscopic techniques such as RAMAN and XRD, and a comparison with SAED results has been also performed. The second part of the *Chapter* has provided a detailed nanostructural characterization of the samples by using TEM related techniques. The aim of this part has been to establish a relationship between the macroscopic effects that surround the

phase transition and growth mechanisms with the nanoscopic changes observed, such as Nb segregation during phase transition. Furthermore, the TiO_2 grain size evolution with Nb loading percentage at low (600 ºC) and high (900 ºC) annealing temperatures has been also studied.

In *Chapter 4* we have studied the Pt/TiO_2 systems. In this case, Pt nucleates on TiO_2 surface as metal nanoclusters. This *Chapter* has been devoted to study the *Superficial Clustering*, as another of the possibilities for additive distribution on semiconductor nanopowders. Since in this case the semiconductor nanopowders structural phase remains stable at the growing conditions used and it is not affected by metal loading we have just given a brief scope of the spectroscopic results at the beginning of the *Chapter* and we have centered our efforts in the nanostructural and morphological characterization of the samples by the TEM related techniques. Moreover, the last part of the *Chapter* has been devoted to analyze the platinum distribution on titania nanopowders using the experimental information obtained from TEM and ICP techniques. A brief description of the Macro-Agglomeration phenomena is also given.

In *Chapter 5*, the metal/semiconductor system selected has been the Pd/SnO_2. Palladium atoms can remain atomically ultradispersed on SnO_2 surface, as it will be showed. This *Chapter* has been devoted to the study of the *Metal Ultradispersion*. In this case we have analyzed the evolution of metal dispersion from low to high doping values. In a first part, for low loading values, the use of in-situ and ex-situ reducing methods have allowed us to reproduce the conditions experimented by the nanopowders during gas sensing, what has given the opportunity of evaluating and analyzing the nanostructural changes concerning to the metal loaded. In the case of high metal loading values we have reported the influence of the excess of Pd on the SnO_2. The samples have been also studied as-grown and after ex-situ reducing process. At the end of the *Chapter*, the experimental results at nanoscopic scale have been related to the macroscopic electrical response given by a sensor device using the same material and tested in our Department.

The application of the TEM nanoscopic related techniques (such as HRTEM, DIP and CIS) to the sample analysis has allowed us to study several aspects of the sensing phenomena at the atomic scale. All these techniques have been presented as powerful and necessary for future studies if a perfect comprehension of the gas sensing mechanisms in SGS materials wants to be performed.

Finally in *Chapter 6*, the main conclusions of this work and the proposals for future studies have been briefly summarized.

1. State of the Art:

Metal additives in semiconductor gas sensors

1.1 General Approach to Semiconductor Gas Sensors

Nowadays, there is a great interest in implementing sensing devices in order to improve environmental and safety control of gases. There is also a great needing of this kind of sensors to carry out the optimization of combustion reactions in the emerging transport industry and in domestic and industrial applications.

The most used gas sensor devices can be divided in three big groups depending on the technology applied in their development: Solid State, Spectroscopic and Optic.

Spectroscopic systems are based on the direct analysis of the molecular mass or vibrational spectrum of the target gas. These sensors can measure quantitatively the composition of the different gases with a good precision. Mass chromatography and mass spectrograph are maybe the most important gas sensor spectroscopic systems.

Optical sensors measure absorption spectra after the target gas has been stimulated by light. This kind of sensors requires a complex system: a monochromatic excitation source and an optical sensor for the analysis of the absorbed spectra.

While spectroscopic and optic systems are very expensive for domestic use and sometimes difficult to implement in reduced spaces as car engines, the so-called Solid State sensors present great advantages due to their fast sensing response, simple implementation and low prices [1, 2, 3]. These last Solid State gas sensors are based on the change of the physical and/or chemical properties of their sensing materials when exposed to different gas atmospheres. Although the number of materials used to implement this kind of devices is huge, this work will be centered in

studying the ones based in semiconductor properties, and more specifically in those using TiO_2 and SnO_2 as sensing materials.

These Semiconductor Gas Sensors (SGS) present the property of changing the conductivity of the sensing material in presence of a determinate gas [4]. The working temperature at which these devices are more efficient can vary depending on the gas atmosphere and on properties of the sensor material selected in every case. As these temperatures range from 200 to 800 ºC, far from room temperatures, it is necessary to implement a heating system in sensor devices. A simple SGS will be composed of a substrate (where sensor material will be supported), the electrodes (to measure the conductivity changes) and the heaters (to reach the optimum sensing temperatures). A simple scheme is shown in *figure 1.1* [5].

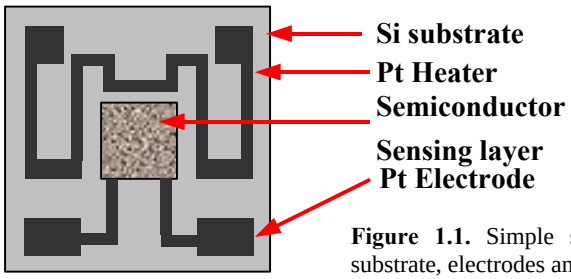

Figure 1.1. Simple scheme of SGS with Si substrate, electrodes and heater resistance.

The main part of efforts made nowadays in SGS research field are in the way of solving the problems that these materials can present. There are three parameters we should improve in order to obtain an accurate device: its sensitivity, its selectivity and its stability [5, 6].

Sensitivity

This is the device characteristic of percepting a variation in physical and/or chemical properties of the sensing material under gas exposure. In order to improve it, it will be of great interest to work with the most appropriate sensing material in every case, and reach its optimum detecting temperature. As suggested by several authors [7, 8], working with

nanostructured materials will give a higher surface area in front of gas. Taking into account that sensing reactions take place mainly on sensors layer surface, the control of semiconductor particle size will be one of the first requirements for enhancing the sensitivity of the sensor.

Selectivity

This characteristic is related to the discrimination capacity of a SGS device in front of a mixture of gases. As it is well known, we can obtain almost the same conductivity value for different gas species and concentrations. One of the possible solutions to this problem would be the mathematical treatment of every sensor signal and the different responses of a sensor array [9, 10]. On the other hand, we could also change the sensor transducer function, introducing electronic elements to our integrated devices [11]. Both possibilities wouldn't modify our sensing material, but would increase the complexity of devices. Thus, in order to simplify device implementation it is interesting to modify material characteristics for example by introducing catalytic additives, which can enhance the material activity toward determinate gas species and reduce it for the rest [12, 13, 14, 15, 16, 17, 18, 19, 20]. The catalytic additive introduction will be treated deeply in further chapters.

Stability

It is a characteristic that takes into account the repeatability of device measurements after a long use. To avoid the effects of non-repeatability after repeated use, several SGS manufacturers [21, 22] submit these materials to a thermal pre-treatment, which would decrease posterior material instabilities. During these treatments samples are submitted to high calcination temperatures (from 400 to 1000 ºC during 1 to 8 hours) to avoid instabilities during their working life, continuously heated at 200-400 ºC.

1.2 Semiconductor Sensing Materials: SnO_2 and TiO_2

1.2.1 General Properties of Sensor Materials

As mentioned above, the interest of sensing materials consists in the change of their electrical properties in presence of a determinate gas. Depending on the materials, this change can be due to *Surface Conductance Effects* or *Bulk Effects*. Nevertheless, not only sensing properties are interesting, but also the stability of the material. In this case bulk properties have also to be taken into account. In this work, we will study the most common materials used: SnO_2 for surface and TiO_2 for bulk conductance sensing mechanisms. Whereas SnO_2 presents the maximum of sensitivity at 200-400ºC exhibiting poor sensitivity and low stability at higher temperatures, TiO_2 will be perfect to work in high temperature environments [5]. Moreover, depending on the gas species to be detected and the environmental working conditions (as temperature) we will use a determinate species as SGS material.

1.2.1.1 Surface Conductance Effects

In the case of detecting oxidizing or reducing gases in the range of 200-400 ºC, a good candidate will be SnO_2. In *figure 1.2.1* we show a schematic drawing of the gas sensing phenomena on Tin dioxide (SnO_2). Notice that sensing phenomena mainly takes place on materials surface.

In order to describe the surface conductance effects in front of gases we have taken the simplest example, as is the case of H_2 acting as a reducing gas. The dependence of the electrical conductivity s on hydrogen partial pressure p_{H_2} can be characterized by a parameter m_s as defined by Radecka et al. [23] as,

$$m_s = \left(\frac{\partial \log s}{\partial \log p_{H_2}} \right)^{-1} \quad (1.1)$$

The theoretical values of m_s can be found depending on the gas-solid state interaction occurred on the semiconductors surface.

Under the presence of O_2 in atmosphere, the sensing material chemisorbs it on its surface. Oxygen can be adsorbed in several forms such as: O_2^-, O^-, O^{2-}. The interaction between a semiconductor surface and H_2 (with reducing properties) can be explained in terms of the reaction of hydrogen molecules with the preadsorbed oxygen. The following reactions could be proposed:

$$O_2^- + 2H_{2(g)} = 2H_2O_{(g)} + e^- \quad (1.2)$$

$$O^- + H_{2(g)} = H_2O_{(g)} + e^- \quad (1.3)$$

$$O^{2-} + H_{2(g)} = H_2O_{(g)} + 2e^- \quad (1.4)$$

Applying the mass-action law to *Expressions* (1.2)-(1.4) gives:

$$n = \frac{K_2}{\left[p_{H_2O}\right]^2} p^2{}_{H_2} \quad (1.5)$$

$$n = \frac{K_3}{p_{H_2O}} p_{H_2} \quad (1.6)$$

$$n = \left[\frac{K_4}{p_{H_2O}} \right]^{1/2} p_{H_2O}^{1/2} \quad (1.7)$$

where n denotes the concentration of electrons and K_2, K_3 and K_4 are the equilibrium constants of expressions (1.2)-(1.4), respectively. It has been assumed that the concentration of adsorbed oxygen remains constant during its interaction with hydrogen. This is justified by $p_{O_2} >> p_{H_2}$ and a high rate of oxygen chemisorption under the experimental conditions.

As the electron mobility m is practically independent of the gas composition and the relationship $s = emn$ holds for n-type semiconductors, the $s(p_{H_2})$ dependence assumes the same form as $n(p_{H_2})$ described by the

expressions (1.5)-(1.7). Thus, m_s = ½ 1 or 2 have been theoretically predicted for the different oxygen species preadsorbed on the semiconductor surface [23].

Attending to the SnO_2 response in front of the different gas species, we can divide them in two different groups: in the first group there are included those gases as CO, H_2 and CH_4 which have got reducing properties and lead to a increase on material conductivity. In a second group, there are those gases like NO_2 and CO_2 that have oxidizing properties and lead to an oxidation of material, reducing its conductivity.

Nevertheless, at elevated temperatures it has been generally recognized that SnO_2 has poor selectivity and low thermodynamic stability [23]. On the other hand, other materials as TiO_2 that base its sensing properties in the changes on volumic conduction can work at high temperatures. All this features have been detailed in the following *Section*.

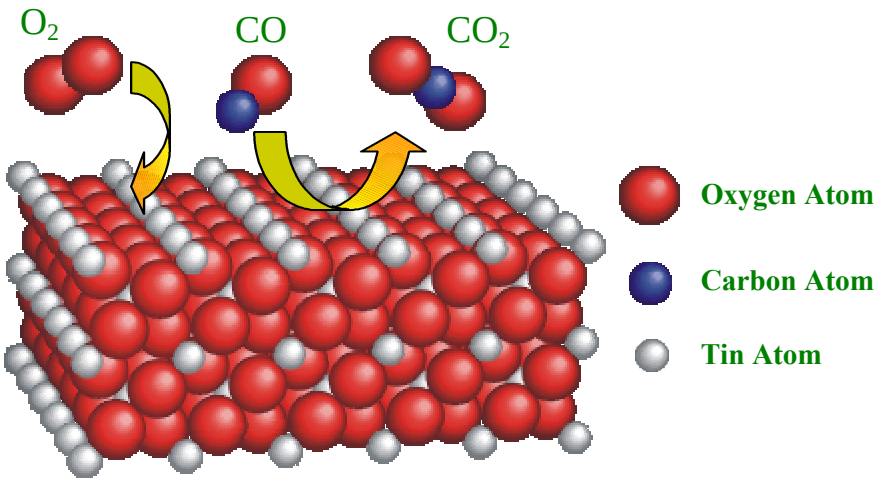

Figure 1.2.1. We present a scheme of the SnO_2 acting as semiconductor sensing material. O_2 molecules present in atmosphere are chemisorbed in material while CO adsorbs O atoms from surface becoming CO_2.

1.2.1.2 Bulk Conductance Effects

TiO_2 will be the perfect candidate for O_2 sensing in combustion processes where the SGS device has to work at high temperatures (600-1000

ºC) [24]. TiO_2 shows high sensitivity towards oxygen gas, and especially when it is doped with metal impurities as Nb [25].

TiO_2 responds to changes in oxygen partial pressure in the upper temperature range (700 ºC and above) and reflects the equilibrium between the atmosphere and its bulk stoichiometry [26, 27] (see scheme in *figure 1.2.2*).

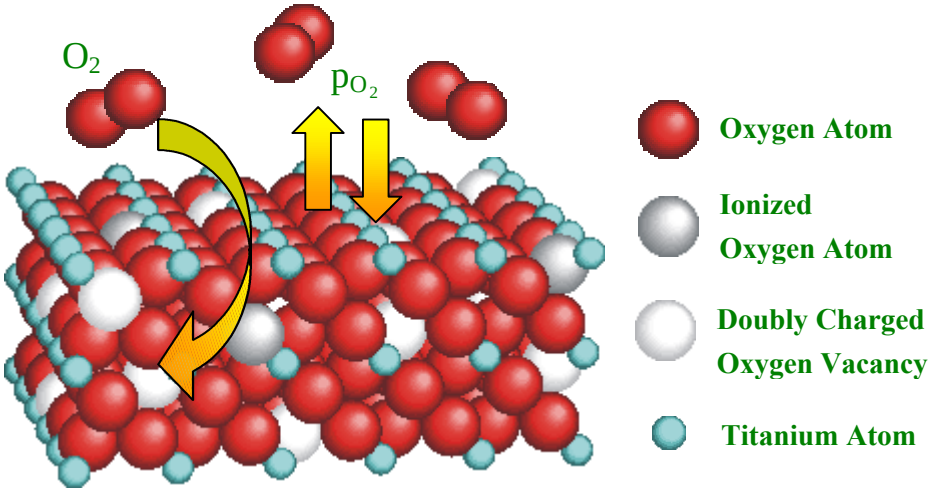

Figure 1.2.2. Scheme of the TiO_2 bulk sensitive properties. SGS respond to oxygen partial pressure changes in the upper temperature range (700 ºC) and reflects the equilibrium between the atmosphere and its bulk stoichiometry.

In general, the relationship between oxygen partial pressure and the electrical conductivity of a mixed valence oxide sensor may be represented by [26, 28],

$$s = A\exp(-E_A/kT)p_{O_2}^{1/N} \qquad (1.8)$$

where *ó* is the electrical conductivity, A is a constant, E_A is the activation energy for conduction, p_{O_2} is oxygen partial pressure and N is a constant determined by the dominant type of bulk defect involved in the equilibrium between oxygen and the sensor. In the case of TiO_2 at high temperature, the

principal defect may be a doubly charged oxygen vacancy, $V_{\ddot{O}}$, replacing an occupied oxygen site, O^x, then the equilibrium can be written

$$O^x \overrightarrow{\leftarrow} V_{\ddot{O}} + \tfrac{1}{2} O_2 + 2e^- \qquad (1.9)$$

so that the equilibrium constant is

$$K = [V_{\ddot{O}}][e]^2 \left[p_{O_2}\right]^{1/2} \qquad (1.10)$$

where [*e*] is the concentration of electrons. Now, for charge balance $[V_{\ddot{O}}] = 2[e]$, so the *expression 1.10* becomes,

$$K = [2e][e]^2 \left[p_{O_2}\right]^{1/2} \qquad (1.11)$$

and hence $[e] \propto p_{O_2}{}^{-1/6}$, i.e., N = -6

Other types of defect lead to other values of N [29], as we will show for the case of Nb diffusion induced defects, where N = -4 (as explained in *Chapter 3*).

Since the main objective of our work is not the description of the basic sensing phenomena but the disposition of the catalytic elements when added to SGS materials, we will not deal further with this fundamental knowledge. Further explanations about SGS materials properties, and especially about tin dioxide, are given in Diéguez and Cirera Ph.D. Thesis, references [5] and [30] respectively. However, as far as the structural properties are concerned, since they will be used in future chapters for Transmission Electron Microscopy (TEM) analysis and Computer Image Simulation (CIS), they will be exposed in some detail.

1.2.2 Crystalline Structure of SnO_2

In the recent years, owing to its chemical and mechanical stabilities, tin dioxide (SnO_2), which is a wide energy gap n-type semiconductor, has been used to develop gas sensors based in thick film polycrystalline material or small particles [31, 32, 33].

Tin (IV) dioxide (II) or SnO_2 has only one stable phase, the so-called cassiterite (mineral form) or rutile (material structure). It crystallizes in the

tetragonal Rutile structure with space group $D_{4h}^{14}\left(P4_2/mnm\right)$, which corresponds to number 136 in the standard listing, see *figure 1.3* for the schematic rutile structure. Its unit cell contains six atoms (two tin atoms and four of oxygen). Tin atoms occupy the center of a surrounding core composed of six oxygen atoms placed approximately at the corners of a quasi-regular octahedron. In the case of oxygen atoms, three tin atoms surround them, approximately forming an equilateral triangle. The metal atoms (Sn^{4+} cations) are located at (0,0,0) and (½,½,½) positions in the unit cell, and the oxygen atoms (O^{2-} anions) at ±(*u*,*u*,0) and ±(½ − *u*,½ + *u*,½), where the internal parameter *u*, takes the value 0.307. Lattice parameters are: *a* = *b* = 4.7382 (4) Å and *c* = 3.1871 (1) Å with *c*/*a* ratio of 0.6726 [30, 34].

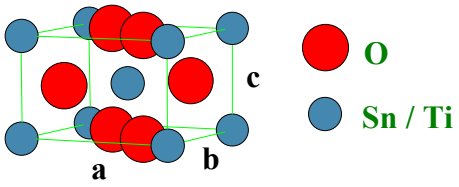

Figure 1.3. Rutile structure for crystalline SnO_2 or TiO_2.

1.2.3 Crystalline Structure of TiO_2

TiO_2 is extensively used in gas sensing because of its desirable sensitivity and mainly because of its good stability in adverse environments [35, 36, 37]. Titanium (IV) Oxide (II) has one stable phase, rutile (tetragonal) and two metastable polymorph phases, brookite (orthorhombic) and anatase (tetragonal). Both metastable phases become rutile (stable) when submitting the material at temperatures above 700 ºC (in pure state, when no additives have been added) [38]. All the TiO_2 samples analyzed in the present work were firstly synthesized from anatase phase and submitted to a calcination process in order to reach the stable rutile phase. Brookite phase never appeared in our sensing materials, thus it will be excluded from

properties summary and we will just give a brief sum up of crystal and structural properties of anatase and rutile phases.

1.2.3.1 TiO_2 in Anatase Metastable Phase

The anatase polymorph of TiO_2 is one of its two metastable phases together with brookite phase. For calcination processes above 700 ºC all anatase structure becomes rutile [39]. Some authors also found that 500 ºC would be enough for phase transition from anatase to rutile when thermal treatment takes place in H_2 (reducing environment) [40]. Anatase structure is tetragonal, with two TiO_2 formula units (six atoms) per primitive cell. The space group is $D_{4h}^{19}\left(I4_1/amd\right)$, which corresponds to number 141 in the standard listing [41], see *figure 1.4* for the schematic anatase structure. The metal atoms (Ti^{4+} cations) are located at 4(b) sites: $\left(0, \frac{1}{4}, \frac{3}{8}\right)$ in the unit cell.

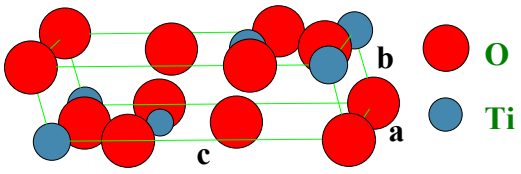

Figure 1.4. Anatase metastable phase for crystalline TiO_2.

The oxygen atoms (O^{2-} anions) are placed at 8(e) sites: (0, ¼, *z*), where the internal parameter *z*, takes the value 0.1656(5). Lattice parameters are: $a = b = 3.7710\ (9)$ Å and $c = 9.430\ (2)$ Å with *c*/*a* ratio of 2.5134, [42, 43].

1.2.3.2 TiO_2 in Rutile Stable Phase

The stable phase of TiO_2 corresponds to the rutile structure or titania. The space group and atoms location sites correspond to those presented above for the SnO_2 in rutile phase, changing the Sn^{4+} metallic cation by Ti^{4+}. The rutile structure was schematically drawn in *figure 1.3*. The lattice parameters correspond now to $a = b = 4.5933$ Å and $c = 2.9592$ Å with *c*/*a* ratio of 0.6442, [38, 44].

1.2.4 Usual Techniques for SnO_2 and TiO_2 Production

The most extended technologies that are used for metal oxide production in nanophase state are divided in two groups. In the first group there are the so called chemical methods: Sol-gel [45], Spray Pyrolisis [46] and Microwave [47]. In a second group there are those techniques based in physical properties as Sputtering [48].

Sol-gel

From a chlorate precursor of the metal specie (Ti or Sn), and after chemical processing, a metal hydroxide precipitate (Sol) will be obtained. Chlorate precursors used for this technique vary depending on the author: for example, while Zhu et al. [49] and Kappler et al. [50] use simple metal chlorates ($PtCl_4$ and $SnCl_4$ respectively), other authors prefer to use some other complex precursors as titanium butoxide ($Ti(OC_4H_9)_4$) or tin chloride alkoxides $SnCl_x(OC_3H_7)_{4-x}$, [51] and [52], respectively. Then, after drying the Sol hydroxide (at about 60 ºC) the resultant Gel will be calcinated to reach the final nanophased material. The procedure followed can be schematized as follows,

$$SnCl_4 + 4NH_4OH \rightarrow Sn(OH)_4 + 4NH_4Cl \qquad (1.12)$$

After calcination of the final product shown in the expression above, the nanophased material will be obtained. Sometimes, the material obtained will need a grinding process in order to separate agglomerated particles and reduce its size [53, 54]. Nevertheless, grinding processes can introduce defects. Dislocations and deformation twins were found by Suziki et al. in SnO_2 and TiO_2 crystals with rutile structure after grinding [55].

Spray Pyrolisis

The chemical metal precursor, usually a chlorate, is pulverized or sprayed on a heated substrate, where a pyrolytic reaction takes place and

nanocrystalline metal oxide is produced. The usual expressions for this reaction are:

$$SnCl_4 + 2H_2O \rightarrow SnO_2 + 4HCl \quad (1.13)$$

$$SnCl_4 \cdot 5(H_2O) \rightarrow SnO_2 + 4HCl + 3H_2O \quad (1.14)$$

Further details of this technique can be found in Correa-Lozano et al. work [56].

Microwave

This procedure consists on the irradiation with microwaves of a solution containing the tin chloride. This innovative technique requires the use of microwave energy with a frequency of 2.45 GHz, which produces doped or undoped powder precursors in just a few minutes. After this irradiation, pseudo-crystalline tin oxide is obtained. Further stabilization treatments (conventional heating, OH-stimulated microwaves and combined treatments) have to be also carried on. Reproducibility, low cost and suitability for mass production demonstrate the industrial and scientific feasibility of this new procedure. This technique was developed, for SnO_2, as a primacy in our laboratory, and it has been reported and explained extensively in previous works [5, 47].

Sputtering

Nowadays, this is one of the most used techniques to synthesize SGS materials. Consist basically on the pulverization with an ion beam from a target containing the material to be deposited. The structure of metal oxide deposited is influenced by the substrate used for this deposition [57]. It is important to notice that this technique allow us to control precisely our semiconductor layer thickness. Thin SGS layers used in microelectronic devices will increase dramatically sensor sensitivity due to their reduced thickness [58, 59]. The implementation of this technique is very expensive for academic research, and it is mainly used in industry, where massive implementation on silicon microsensors wafers can reduce prices.

1.3 Metal Additives Introduction in SGS Materials

1.3.1 General View

Transition metal oxides, such as TiO_2, SnO_2, WO_3, In_2O_3, etc. appear to be the best candidates for semiconductor gas sensors [1, 2, 60]. The sensitivity of these devices is based on the dependence of the conductivity of metal oxides on the surrounding atmosphere. Nevertheless, full development of such devices requires an improvement of their characteristics by the introduction of metal additives [61]. These additives enhance the material sensitivity and selectivity, and decrease the response time and the operating temperature of the sensitive layer [62, 63]. To increase the sensitivity and selectivity, one of the most widely used methods has been the addition of catalytically active metals, such as Pt and Pd [53, 64, 65, 66] or even Au [67], which have been claimed to promote chemical or electronic sensitizations [68, 69]. Loading of other elements such as, for example, Sb or La, change mainly the doping level, thus, modifying the bulk Fermi level position and, hence, the equilibrium carrier population at the grain surfaces [30]. The addition of the different metallic species to semiconductor gas sensing materials will improve the gas detection of a determinate gas in every case. See in *table 1.1* a report of the sensing semiconductor materials and the corresponding target gases they have been used to detect.

Target Gas detected	Metal Additive/SC used	References
LPG (Liquid Petroleum Gas)	Pd / SnO_2	[70, 71]
CO	Pd / SnO_2 Pt / SnO_2	[46, 47, 52, 54, 70, 72, 73, 74, 75, 76] [46, 47, 72, 75, 76]
CH_4	Pd / SnO_2	[54, 70, 77, 78]
H_2	Pt / SnO_2 Pd / SnO_2 Pt / TiO_2 Nb / TiO_2	[17, 79] [17, 79, 80, 81] [17, 82] [19]
NH_3	Pt / TiO_2	[82]
O_2	Pd / SnO_2 Nb / TiO_2 TiO_2 high temperature	[17, 81] [19, 20] [82]
Ethanol/Methanol	Pt / TiO_2 Pd / SnO_2 Nb / TiO_2	[51] [83, 84] [51]
NO_2	Pd / SnO_2 Pt / SnO_2	[47, 52, 53] [53]

Table 1.1. Report of the sensing semiconductor materials and the corresponding target gases they have been used to detect.

Another important property is that the presence of metallic additives can also modify the growth kinetic, as was previously observed by some other authors [69, 85]. In a recent work [86], we found that important changes in SnO_2 nanopowders growth kinetics could be induced by the addition of platinum and palladium. For both additives, we observed a dependence of the SnO_2 grain size on the used metal concentration. The higher the concentration was, the lower was the resulting grain size. However, two differentiated regions were observed for the grain growth behavior, below and above 900°C treatment temperatures. On the other

hand, gold did not introduce any significant change. The obtained size for the nanopowders with gold did not depend on the gold concentration.

In order to load these metallic additives to the semiconductor metal oxide, a wide diversity of technologies have been used. In *table 1.2* there is a report of the most common technologies used recently in the different laboratories and companies.

Technology used for additive loading	Metal Additive/SC	References
Laser Induced Pyrolisis	Nb, V, Ta / TiO_2	[87, 88]
Sputtering	Ce, Nb, Cr, Cd / TiO_2 Pt, Pd, Au / SnO_2	[48, 57] [84, 89]
Impregnation	Pt / TiO_2 Pt, Pd / SnO_2 Pd / MgO	[13, 90] [89, 91] [92]
Sol-gel	Pd / SnO_2 Nb / TiO_2	[52, 93] [20]
Microwave	Pt, Pd / SnO_2	[5, 47]
Electron Beam Evaporation	Pt, Pd / SnO_2	[94]
Pulsed Laser	Pt / TiO_2 Pt, Pd / Si, C	[37, 95] [96]
Metal Vapor Synthesis	Pt, Pd / *	[97, 98]
Flowing Gas Mixture	Pd / Ln_2O_3	[99]
Photoreduction + Precursor Adsorption	Pt / TiO_2	[100, 101, 102, 103]
Open-circuit Potential	Pt / TiO_2	[104]
Metal Organic Chemical Vapor Deposition	Nb, V / TiO_2	[105, 106]

Table 1.2. Report of the most common technologies used recently in the different laboratories and companies for metal additive loading.

Due to the variety of additives studied in this work, several techniques have been used to load them (Impregnation, Sol-gel, Electroless,

etc.). A brief explanation of the specific technology used for metal additive loading in our samples will be given in the experimental part of the implied chapters.

1.3.2 Additive Disposition in Semiconductor Gas Sensing Material

The amount and distribution of the metal is the most important parameter to be controlled in order to obtain the highest sensitivity [107]. When loading metal additives to semiconductor materials, on one hand, it is generally expected to find this metals promoting a dopant effect. This is the case of Nb and Ce loaded to TiO_2, which diffuse entering substitutionally inside semiconductor bulk or occupying interstitial positions or inducing structural changes in metal oxide structure [48, 108]. On the other hand, people working in catalysis would expect a metal cluster or nanocluster formation on semiconductor nanopowders surface, such as those observed in the case of Pt [109, 110] and Pd [111, 112]. Although these are the general thoughts about additive disposition, these metals can also be distributed in other ways. Sometimes, when the metal is loaded in low concentrations it can be dispersed as monoatomic centers, the additive metal is then ultradispersed or atomically dispersed on semiconductors surface, as found in the case of Pd over SnO_2 [94, 113]. In the opposite way, metal distribution can lead to the formation of macro-agglomerated metal clusters as big as semiconductor grains, as found in the case of Au loaded to SnO_2 [86] and Pt to TiO_2 [114, 115, 116]. In *figure 1.5*, a schematic representation of all these additive distribution patterns is drawn[♣].

In the following, we will try to accurately describe all these additive disposition patterns, and give the most interesting properties that each one carry to gas sensing and catalysis.

[♣] The *atomic element color code* used in the schemes presented in *figure 1.5* has been applied to the rest of cell and supercell models presented in this work.

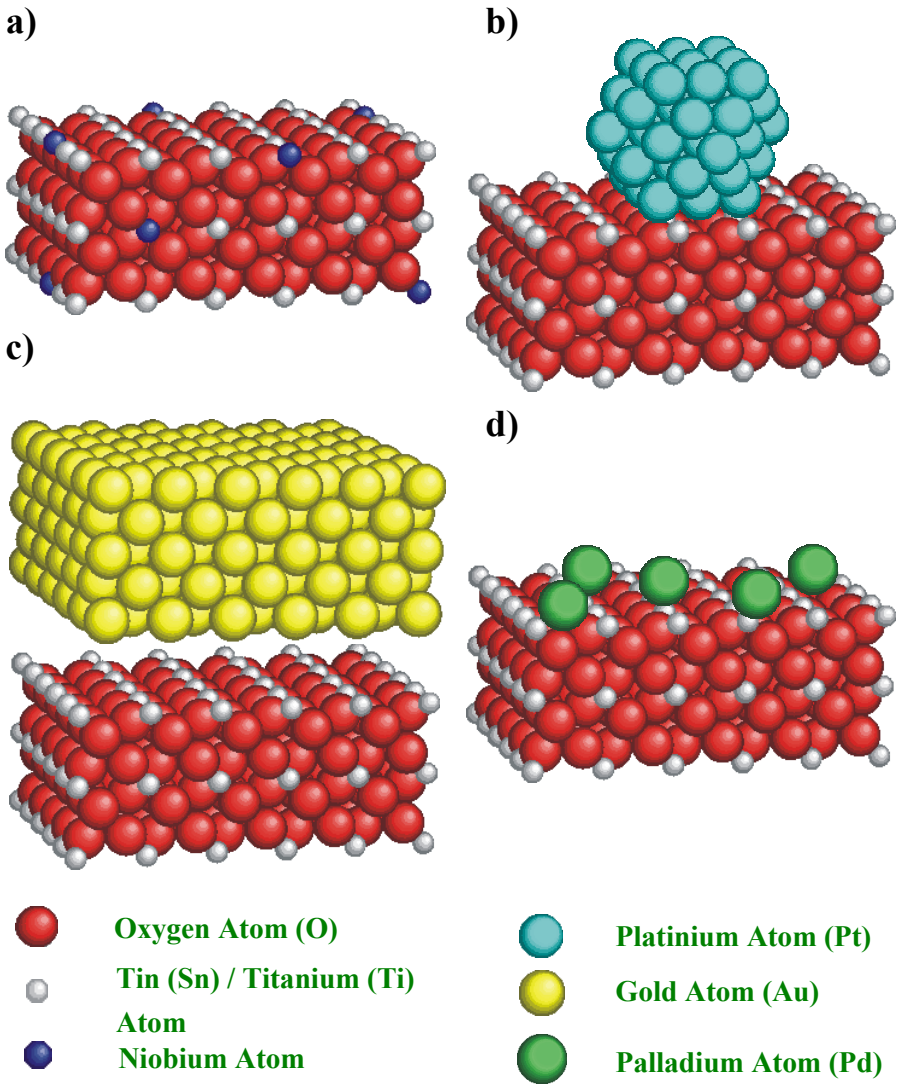

Figure 1.5. A schematic representation of additive distribution ways on SGS material structure (SnO_2 or TiO_2) is drawn. **a)** Metal bulk diffusion, with Nb metal atoms inside TiO_2 bulk. **b)** Superficial clustering is represented showing a 55-atoms cuboctahedral Pt nanocluster on SnO_2 or TiO_2 rutile surface. **c)** Macro-agglomerated metal, showing metal additive clusters (Au) as big as metal oxide grains. **d)** Atomically Ultradispersed metals, with several Pd atoms on SnO_2 surface.

1.3.2.1 Metal Diffusion inside Semiconductor Bulk

The first option for additive distribution is the metal diffusion inside semiconductor bulk, occupying interstitial or substitutional positions or inducing structural changes in metal oxide structure, as in the case of Nb, V and Ce loaded to TiO_2 [48, 106, 108]. As a consequence of this loading, the optical and electrical properties of the support material change. Mardare et al. [48] found that while undoped TiO_2 crystallized in a mixed rutile/anatase phase at 250 °C, the doped materials exhibited the anatase phase only. It is also common to introduce Nb to TiO_2 crystals to provide an increase in its conductivity [117]. One of the most used applications for Nb/TiO_2 materials are oxygen detectors due to their lower reference signal R_0 and one-to-one correlation between R (response) and p_{O2} (oxygen partial pressures).

Furthermore, great interest is devoted to the kinetics of grain growth and to the potential identification of the inhibitors of grain growth in nanocrystalline TiO_2 nanophases [87]. In these studies, the presence of different metals, such as V, Nb, Ta, Al and Ga, in the TiO_2 powders has been correlated to the temperature of the anatase-rutile transformation and to the microstructural parameters of the mixed oxide powders before the thermal treatments. Unlike V which inhibits the growth only of anatase, the other metals (Nb, Ta, Al and Ga) inhibit the growth of both anatase and rutile, which show similar growth kinetics.

Actually, there is a considerable interest in the effect of chemically inequivalent foreign atoms on the surface reactivity of TiO_2. It is highly desirable to chemically incorporate the foreign atoms without changing the crystallographic structure of TiO_2 rutile. Nb and V (group V A transition metals) have one additional valence electron (Nb^{5+} and V^{5+}) compared to Ti (Ti^{4+}), and their ionic radii are close to that of Ti^{4+} [105]. Thus, both are excellent candidate foreign atoms for isostructural incorporation into the TiO_2 anatase or rutile lattice. In this way, Sharma et al. [24, 25] also suggested that the possible incorporation of Nb in TiO_2 structure was like Nb^{5+} ions. These Nb^{5+} ions would achieve the charge neutrality in pure TiO_2,

compensating doubly charged oxygen vacancies, and improving the sensitivity and response time of sensor device.

Controversially, several other authors have suggested that the oxidation state of both Ti and Nb is 4+ [105, 118]. In this case, Nb atoms would substitutionally incorporate at cation sites in the rutile lattice ($Ti_{1-x}Nb_xO_2$) for *x* up to 0.4 (the highest value in these previous studies). In these works, they found that the cause for Nb^{4+} could be attributed to the epitaxial growth of the doped TiO_2 because both TiO_2 and NbO_2 can form the rutile structure and exhibit a complete solid solution with each other.

Nevertheless, other authors studied the growth scenario of Nb/TiO_2 finding that not interdiffusion of Nb in TiO_2 existed. In this way, Marien et al. [119] recently studied the growth, structure and chemical composition of the interface between the strongly reacting metal Nb and TiO_2. They found that Nb did not diffuse, but remained on TiO_2 surface forming a thin film. Experimentally, they showed that the first two monolayers of Nb in contact with TiO_2 were oxidized. However, they couldn't determine whether NbO, NbO_2 or Nb_2O_5 was formed.

In the *Chapter 3* of this thesis several nanocrystalline TiO_2 specimens loaded with Nb will be studied in order to find the possible Nb interdiffusion, segregation on TiO_2 surface or formation of intermetallic $Ti_{1-x}Nb_xO_2$ alloys.

1.3.2.2 Superficial Clustering

From catalysis point of view, it is generally expected that metal additive loading will imply the formation of nanoclusters on metal oxide surface. In this way, several authors pointed that this effect mainly happens in the case of noble metal loadings [94, 120, 121, 122, 123]. The typical sizes of these nanoclusters range from 1 to 8 nm in diameter. Both Pt and Pd provide effective catalytic adsorption sites for oxygen and reducing gases and nucleate on metal oxide surface. The main difference between Pt and Pd is that Pd forms a stable compound with oxygen whereas Pt does not form a stable compound around the temperatures used in sensing [69]. As a result,

part of the Pt remains in a metallic state in air, providing not only catalytic adsorption sites for oxygen but also helping spillover of activated oxygen species onto metal oxide surface where they get ionosorbed by trapping electrons from the metal oxide (in our case, SnO_2 or TiO_2). This increase in the density of ionosorbed oxygen species explains the large resistance observed for Pt-SnO_2 film [94]. Under reducing gas environment, the metallic Pt is known to provide preferential catalytic adsorption sites for reducing gas [69]. The surface adsorbed reducing gas further dissociates into more active species at a faster rate and spillover onto metal oxide surface to react with ionosorbed oxygen. This explains the observed rise in sensitivity and fall in response time for Pt-SnO_2 films. Choi et al. observed such a behavior for Pt-SnO_2 films under H_2 ambient [79].

On the other hand, Pd forms a stable oxide in air. It was reported in several works, that Pd oxidation is possible at temperatures as low as 300 ºC in oxygen and consequently, at higher temperature (450-500 ºC), PdO is the predominant species and is the responsible for the catalytic activity [54, 124]. It has also been observed that the work function of the metal oxide changes due to the change in the oxidation state of Pd, as it happens in the case of Pd/SnO_2 [69]. In other words, Pd in the oxygen phase acts as an electron acceptor and traps the charge from metal oxide conduction band. This trapped charge, along with that of ionosorbed oxygen, induces stronger depletion of electrons from the metal oxide surface causing a rise in resistance. Since the depletion of carriers is related to the density of trapped charge at the surface, Pd clusters having a size of a few nanometers are necessary to affect the resistance.

As we explained, the addition of small amounts of noble metals such as Pd and Pt to the metal oxide used for gas sensing can promote not only gas sensitivity but also the rate of response. The promoting mechanisms are not the same for all metals, as Yamazoe et al. demonstrated according to their XPS studies on three different promoters Ag, Pt and Pd in early 90s [69]. They recognized a notable difference among by whether these additives affected the work function of the metal oxide (Ag and Pd) or not (Pt). The

shifts (increase) of the work function, referred to that of unloaded SnO_2, were as much as about 0.7 eV (Ag) and 0.3 eV (Pd) at the respective optimum loadings under oxidizing conditions (in air), while the shifts disappeared completely when the samples were exposed to a reducing atmosphere. They proposed two types of sensitization mechanisms: electronic (Ag and Pd) and chemical (Pt). Both sensitization schemas are shown in *figure 1.6.*

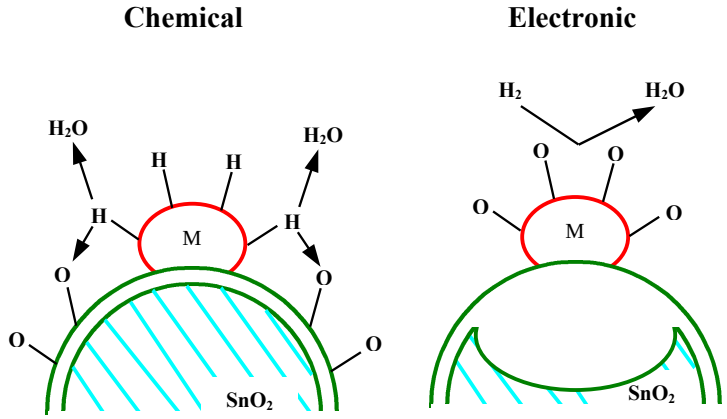

Type	Chemical	Electronic
Role of noble metal	Activation and spillover of sample gas	Electron donor or acceptor
Origin of gas-sensitive properties	Change of adsorbed oxygen concentration	Change of oxidation state of noble metal
Example	Pt-SnO_2	Ag_2O-SnO_2, PdO-SnO_2

Figure 1.6. Both, chemical and electronic sensitization schemas are shown above. After reading [69].

Chemical Sensitization

The chemical sensitization takes place via a spillover effect, which is now rather familiar in catalytic chemistry. The promoter in this case activates a test gas to facilitate its catalytic oxidation on the semiconductor

surface. In other words, the promoter does not affect the resistance of the element directly, leaving the gas-sensing mechanism essentially the same as in the case without it. The promoter increases the gas sensitivity as it increases the rate of the chemical processes leading to a decrease in concentration of the negatively charged adsorbed oxygen. This is why the effect is called chemical sensitization [69, 125].

Electronic Sensitization

On the other hand, electronic sensitization is due to a direct electronic interaction between the metal additive and the semiconductor surface. When the oxidation state of the metal additive changes with the surrounding atmosphere, the electronic state of the semiconductor will also change accordingly. More specifically, the typical additives of this type (Ag and Pd) are known to form stable oxides (Ag_2O and PdO) in air, while they are easily reduced to metals with a reducing gas. The oxidized metal produces a strong electron-depleted space-charge layer inside the semiconductor, inducing shifts in its work-function. However, this electron interaction is ruptured when the oxidized additive is reduced to metal. The absence of the electronic interaction between Pt and SnO_2 seems to reflect that Pt cannot form a stable oxide under these conditions [69].

Obviously Pd particles can be distributed rather uniformly on the spherical surface of each metal oxide particle. Such Pd dispersion, when coupled with the work function changes, allows the mechanism of electronic sensitization to be estimated as shown below (*Figure 1.7*).

In air, the metal additive exists as PdO clusters, which draw electrons from the metal oxide particle underneath and produce an electron-depleted layer in the particle. On exposure to an inflammable (reducing) gas, on the other hand, PdO is reduced to Pd, being accompanied by a decrease or disappearance of the space-charge layer. In this way, PdO nanoclusters play the role of a receptor to the reducing gas, which otherwise is provided by the adsorbed oxygen. The electron affinity of PdO nanoclusters is far stronger

than that of the adsorbed oxygen, leading to the far higher gas sensitivity when working with additive loaded than with unloaded SnO_2.

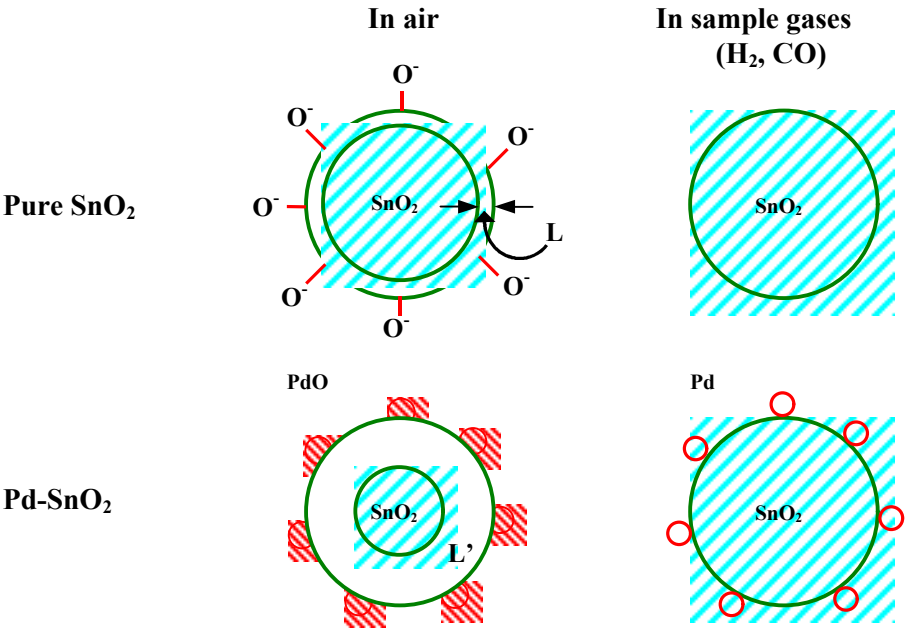

Figure 1.7. Mechanism of electronic sensitization in pure SnO_2 element (upper) and in Pd-SnO_2 element (lower). After reading [69].

Quantum size effects in nanoclusters (up to 561 atoms)

Moreover, when talking about small nanoclusters (up to 561 atoms or approximately 3 nm of diameter), we have to take into account their quantum size effects. The properties of nanometric-scale metallic clusters differ from those of the same material in bulk. Conduction electrons, because of their wave-like nature, can have only certain discrete values of kinetic energy or wavelength. Such 'quantum-size' effects have been observed in two-dimensional electron gases in semiconductors, and in atomic-scale metallic point contacts [126]. Also present are 'Coulomb-charging' effects: these are purely classical in origin and occur when the energy required to add one electron to a conducting sphere exceeds the mean thermal energy. Thermal fluctuations in the total charge on the cluster are then suppressed. In

theory, the combination of quantum-size and Coulomb-charging effects should cause the properties of small metallic clusters to depend sensitively on whether they have an odd or even number of electrons. Odd-even effects have been observed in experiments on tunneling between discrete electronic levels of single metal clusters, but their influence on thermodynamic properties remains to be demonstrated. Volokitin et al. reported measurements of the heat capacity and electronic magnetic susceptibility of small metallic clusters (up to 561 atoms). Their results showed definitive evidence for odd-even effects, thus confirming that quantum and classical size effects strongly influence the thermodynamic properties of small clusters [126].

Moreover, these metallic nanoclusters can also present show size-dependent magnetization. The difference between magnetization measurements on bulk Pd and Pd clusters (if they enter the quantum-size regime) can be explained by quantum-size effects [126**,** 127]. Bouarab et al. [128] presented a theoretical work concerning the onset of magnetism in palladium slabs. Pd slabs with sizes between 2-5 layers should show ferromagnetic behavior [128]. While a monolayer of palladium and slabs with more than 5 layers should not show ferromagnetism. Recently, a more theoretical paper [129] was published which predicts a ferromagnetic behavior of small palladium clusters (Pd_{15} and Pd_{19}, with 15 and 19 atoms, respectively). Until now, there was no evidence that these magnetic properties could affect the catalytic reactions. However, several works have been actually devoted to this study.

Superficial Growing Modes

In order to understand the noble metal disposition on metal oxide surface it will be important to observe and study its growing mode.

Generally, materials deposited on a substrate (support) grow by one of three different modes, that describe the two dimensional growing, the three dimensional, and the mixed mode [130] (see *figure 1.8*). Firstly, in the so-called Frank van der Merwe mode, atoms or molecules grow layer-by-

layer in a sequential fashion, this corresponds to the pure two-dimensional growth, and is characteristic of epitaxial film growth. In contrast, the Volmer-Weber mechanism leads to the formation of individual three-dimensional islands, describing a three-dimensional growth, where nanoclusters are nucleated on surface. And finally, the third mode is a combination of the two, an initial two-dimensional process creates a few monolayers, and then, individual islands form as more material is deposited. This is the mixed model, following both two-dimensional and three-dimensional mechanisms. This process is known as the Stranski-Krastanov mode and is crucial for quantum-dot formation. A necessary condition for growth in this mode is that lattice mismatch of about 4% or more exists between the substrate and the growing film. The wetting layer does not form

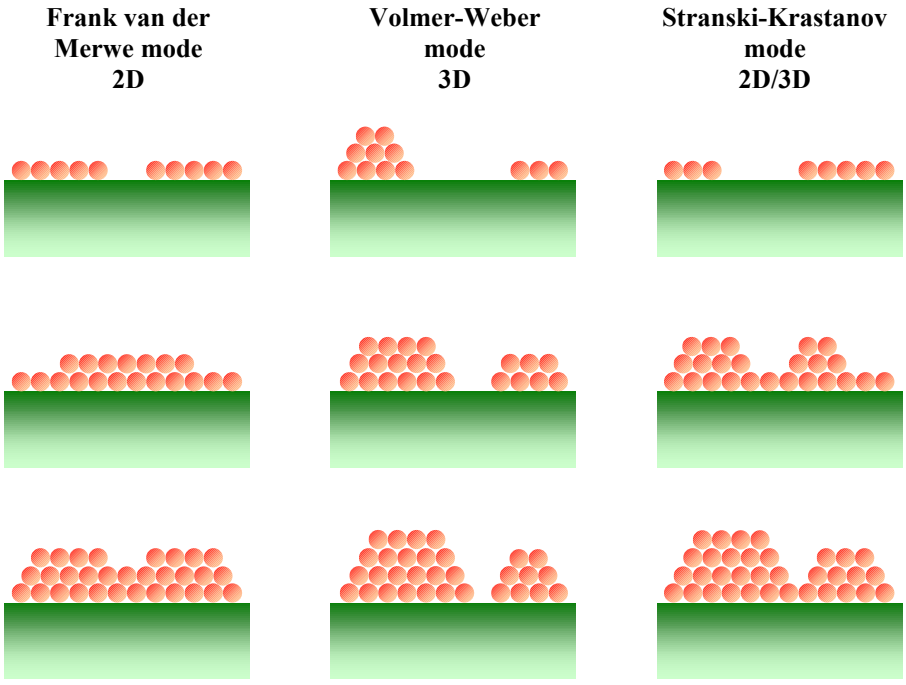

Figure 1.8. The three thin film growing modes. In the two-dimensional Frank van der Merwe mode, layers of material grow on top of each other, atoms or molecules grow layer-by-layer in a sequential fashion. In the Volmer-Weber mode, separate three-dimensional islands form on the substrate. And in the Stranski-Krastanov mode, the critical mechanism for forming quantum dots, one or two monolayers form first, followed by individual islands [130].

when the strain is relaxed by misfit dislocations [130].

In the case of Pt nanoclusters, Suzuki et al. and Petsy et al. suggested a Volmer-Weber three-dimensional growth [131, 132]. At room temperature, Pt grows in three-dimensional islands on the TiO_2 surface, with little indication of an interface reaction.

Another aspect to take in account is that in the Volmer-Weber 3D-growth mode the amount of material loaded on support plays an important role. When a higher amount of metal is loaded to the sample, the cluster sizes become bigger, and eventually merge when metal reaches a critical percentage. In this point it can be almost said that a thin layer of metal covers the support particles, as suggested by Dickinson et al. in their study of Pd growth over TiO_2 substrates [133]. In *figure 1.9* it is shown the merging process when increasing the metal loading.

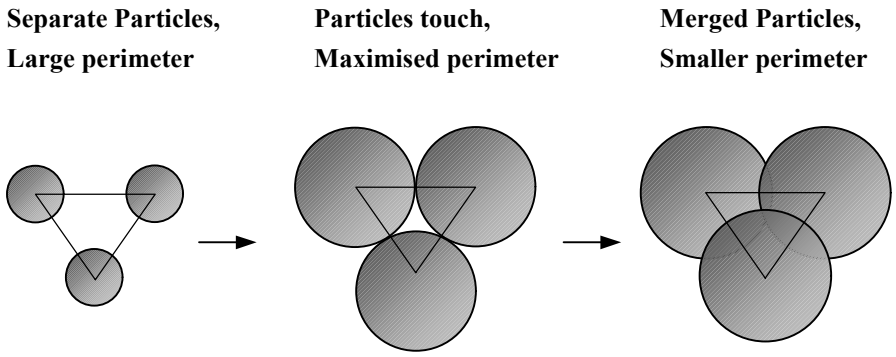

Figure 1.9. Schematic illustration of the effect of particle growth on hexagonally arranged particles. On the left, particles do not touch and the perimeter length is relatively large (and is largest when the particles just touch). On the right, the particles have merged and the perimeter length is significantly reduced [133].

Further studies about material deposition models on support layers are given in next literature references [37, 134, 135, 136].

Metal clustering on metal oxide support will be studied in the *Chapter 4* of this thesis. Several clustering models will be studied, and dispersion statistics will be carried on.

1.3.2.3 Metal Macro-Agglomeration

Metal distribution can be also carried on forming macro-agglomerated metal clusters as found in the case of Au loaded to SnO_2 [86] and Pt to TiO_2 [114, 115, 116]. Pt and specially Au not only nucleates forming small nanoclusters on metal oxide surface, but it also forms independent big clusters with sizes, sometimes, as big as the metal oxide grains (from 50 to 200 nm of diameter). Since metal forming big clusters has a lower effective area involved in gas reactions, it will be of great interest to reduce its quantity obtaining a higher dispersion of Pt nanoclusters on TiO_2 surface.

1.3.2.4 Metal Ultradispersion

When the metal is loaded in low concentrations it can be dispersed as monoatomic centers, the additive metal is then ultradispersed or atomically dispersed on semiconductor surface, as found in the case of Pd over SnO_2 [94, 113] or even sometimes in the case of Pt over TiO_2, although rarely [82]. Composite systems consisting of metal particles interacting with a semiconducting substrate constitute an electron transport system with interesting properties. At very low concentrations when the metal may be dispersed as atomic impurities, the metal may act as a donor or acceptor in the semiconductor. At higher metal concentrations, percolating transitions dominate the electrical behavior of the system.

The most extended opinion found in literature is that while Pt can exist as aggregated metallic Pt clusters, Pd exists as highly dispersed metallic clusters. Zhu et al. [49] found that Pd atoms could enter into the lattice of anatase TiO_2 film. Due to the strong interaction between Pd and TiO_2 film, Pd can exist at the lattice of anatase TiO_2. On the other hand, Pt cannot exist at the lattice of anatase TiO_2 and gather together to form Pt particles. On the contrary, Madhusudhana et al. [94] found that Pd loading did not affect the SnO_2 layer resistance because of the fact that it was distributed most likely in the form of individual atoms and not as clusters.

Using models of Pd adsorption on a SnO_2 (001) slab, Matsushima et al. [137] showed that direct chemical bonding with both covalent and ionic character could be established between the surface O atoms and Pd atoms. In model A, the Pd-related states are present in the band gap, and are atomic-like in nature, thus allowing the ultradispersion. In model B, the Pd-related states have a wide bandwidth because of Pd-Pd interactions. See both models in *figure 1.10*.

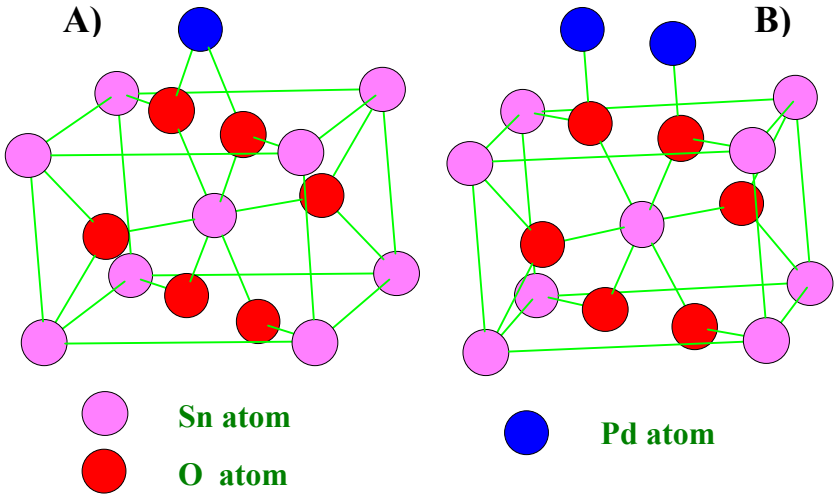

Figure 1.10. Adsorption sites of Pd atoms on a SnO_2 (001) surface. Models A and B. After reading [137].

Several Pd/SnO_2 samples will be studied in the *Chapter 5* of this thesis in order to discuss the effects of ultradispersion in semiconductor gas sensors. The application of in-situ and ex-situ reducing methods will allow us to demonstrate the presence of ultradispersed palladium atoms on our semiconductor grain surfaces. In fact, these reduction processes led to one of the most spectacular results of this thesis work: we will show that the reduction processes can dramatically influence the SnO_2 nanostructure in presence of high Pd concentration, leading to the formation of "doped" SnO_2 stick-like nanoparticles with quasi-wirelike morphology. These SnO_2 nanostructures experimentally obtained are similar to those reported by Pan

et al. [138] in a recent work published in *Science*. They suggested that oxide nanobelts could be "doped" with different elements and used for fabricating nanosized sensors. In this work, we demonstrate that the doping is possible in such special structures, and furthermore sensing response obtained with them is satisfactory as we will show at the end of this *Section*.

References

1. H. Meixner, J. Gerblinger, U. Lampe and M. Fleischer, Thin-film gas sensors based on semiconducting metal oxides, *Sensors and Actuators B*, **23**, 119-125 (1995).

2. T. Takeuchi, Oxygen Sensors, *Sensors and Actuators B*, **14**, 109-124 (1988).

3. J. T. Woetsman, E. M. Logothetis, Controlling Automotive Emissions, *The Industrial Physicist* 20-24, Ed. *American Institute of Physics* (1995).

4. T. Seiyama, A. Kato, K. Fujisishi and M. Nagatoni, A new detector for gaseous components using semiconductive thin films, Analytical Chemistry, **34**, 1052-1053 (1962).

5. A. Cirera, New technologies and their characterization for nanostructured SnO_2 gas sensor devices, *PhD. Thesis*, Universitat de Barcelona, Barcelona (2000).

6. A. Cabot, Additive Effects on Tin Oxide Nanopowders for Gas Sensing Applications, *Research Thesis*, Universitat de Barcelona, Barcelona (2000).

7. Y. Shimizu, M. Egashira, Basic Aspects and Challenges of semiconductor gas sensors, *MRS Bulletin*, **24 (6)**, 18-24 (1999).

8. C. Xu, T. Jun, N. Miura, N. Yamazoe, Correlation between gas sensitivity and crystallite size in porous SnO_2-based sensors, *Chemical Letters*, **3**, 441-444 (1990).

9. S. Marco, A. Cornet, J. R. Morante, E. Castaño, R. Jané, S. Jiménez, A. Pardo, A. Ortega and A. Cirera, Smart multisensor integrating methane and carbon monoxide gas detection with improved selectivity by signal processing, *IGRC'98 Proceedings*, San Diego (1998).

10. T. Šundiæ, Algoritmos cuantitativos de procesado de señal para los detectores de gas de bajo coste, *Research Thesis*, Universitat de Barcelona, Barcelona (1998).

11. D. E. Williams, Semiconducting Oxides as gas-sensitive resistors, *Sensors and Actuators B*, **57**, 1-16 (1999).

12. A. Ueda, T. Nakao, M. Azuma and T. Kobayashi, Two conversion maxima at 373 and 573 K in the reduction of nitrogen monoxide with hydrogen over Pd/TiO_2 catalyst, *Catalysis Today*, **45**, 135-138 (1998).

13. H. Lin, The study of oxygen spillover and back spillover on Pt/TiO_2 by a potential dynamic sweep method, *Journal of Molecular Catalysis A: Chemical*, **144**, 189–197 (1999).
14. J. Sheng, N. Yoshida, J. Karasawa and T. Fukami, Platinum doped titania film oxygen sensor integrated with temperature compensating thermistor, *Sensors and Actuators B*, **41**, 131-136 (1997).
15. M. T. Wu, X. Yao, Z. H. Yuan, H. T. Sun, W. C. Wu, Q. H. Chen and G. Y. Xu, Effect of noble metal catalyst on titania exhaust gas oxygen sensor *Sensors and Actuators B*, **13-14**, 491 (1993).
16. Y. Xu, K. Yao, X. Zhou and Q. Cao, Platinum-titania oxygen sensors and their sensing mechanisms, *Sensors and Actuators B*, **13-14**, 492-494 (1993).
17. K. D. Schierbaum, U. K. Kirner, J. F. Geiger and W. Göpel, Titol: Schottky-barrier and conductivity gas sensors based upon Pd/SnO_2 and Pt/TiO_2 *Sensors and Actuators B*, **4**, 87-94 (1991).
18. J. L. Falconer and K. A. Magrini-Bair, Photocatalytic and Thermal Catalytic Oxidation of Acetaldehyde on Pt/TiO_2, *Journal of Catalysis*, **179**,171–178(1998).
19. K. Zakrzewska, M. Radecka, M. Rekas, Effect of Nb, Cr, Sn additions on gas sensing properties of TiO_2 thin films, *Thin Solid Films*, **310**, 161-166 (1997).
20. M. Z. Atashbar, H. T. Sun, B. Gong, W. Wlodarski, R. Lamb, XPS study of Nb-doped oxygen sensing TiO2 thin films prepared by sol-gel method, *Thin Solid Films*, **326**, 238-244 (1998).
21. Figaro (gas sensor company), Gas Sensor Catalogue and Technical Information (Figaro and Figaro USA, Inc.). http://www.figarosensor.com (2000).
22. Fis (gas sensor company), Gas Sensor Catalogue and Technical Information (Fis, Inc.). http://www.fisinc.co.jp (2000).
23. M. Radecka, K. Zakrzewska and M. Rekas, SnO_2-Tio2 solid solutions for gas sensors, *Sensors and Actuators B*, **47**, 194-204 (1998).
24. R. K. Sharma and M. C. Bhatnagar, Improvement of the oxygen gas sensitivity in doped TiO_2 thick films, *Sensors and Actuators B*, **56**, 215-219 (1999).
25. R. K. Sharma, M. C. Bhatnagar and G. L. Sharma, Mechanism in Nb doped titania oxygen gas sensor, *Sensors and Actuators B*, **46**, 194-201 (1998).
26. P. T. Moseley, Materials selection for semiconductor gas sensors, *Sensors and Actuators B*, **6**, 149-156 (1992).

27. U. Kirner, K. D. Schierbaum, W. Göpel, B. Leibold, N. Nicoloso, W. Weppner, D. Fischer and W. F. Chu, Low and High Temperature TiO_2 Oxygen Sensors, *Sensors and Actuators B*, **1**, 103-107 (1990).

28. Z. Jianzhong, R. Congxin, C. Guoliang, M. Haichuan, W. Jiali, Y. Chunying, Fabrication and characterization of a new automotive air-to-fuel sensors based on Pt- and TiO_2-doped Nb_2O_5 film deposited by IBED, *Sensors and Actuators B*, **46**, 180-185 (1998).

29. P. Kofstad, Non-stoichiometry, Diffusion and Electrical Conductivity in Binary Metal Oxides, *Wiley-Interscience, Ed.*, New York (1972).

30. A. Diéguez, Structural Analysis for the improvement of SnO_2-Based Gas Sensors, *PhD. Thesis*, Universitat de Barcelona, Barcelona (1999).

31. X. Pan and J. G. Zheng, Microstructure of and crystal defects in the nanocrystalline tin dioxide thin films, *Materials Research Society Symposium Proceedings*, **472**, 87-92 (1997).

32. A. Cirera, A. Diéguez, R. Díaz, A. Cornet and J. R. Morante, New method to obtain stable small-sized SnO_2 powders for gas sensors, *Sensors and Actuators B*, **58**, 360-364 (1999).

33. A. Cirera, A. Cornet, J. R. Morante, S. M. Olaizola, E. Castaño and J. Gracia, Comparative structural study between sputtered and liquid pyrolysis nanocrystaline SnO_2, *Materials Science and Engineering B*, **69/70**, 406-410 (2000).

34. *JCPDS*, 41-1445 (1997).

35. K. M. Glassford, N. Troullier, J. L. Martins and J. R. Chelikowsky, Electronic and structural properties of TiO_2 in the rutile structure, *Solid State Communications*, **76 (5)**, 635-638 (1990).

36. A. M. Tonejc, M. Gotiæ, B. Gržeta, S. Musiæ, S. Popoviæ, R. Trojko, A. Turkoviæ, I. Muševiæ, Transmission electron microscopy studies of nanophase TiO_2, *Materials Science and Technology B*, **40**, 177-184 (1996).

37. K. M. Becka, T. Sasakib and N. Koshizakib, Characterization of nanocomposite materials prepared via laser ablation of Pt/TiO_2 bi-combinant targets, *Chemical Physics Letters*, **301,** 336–342 (1999).

38. *JCPDS*, 21-1276 (1997).

39. G. Cerrato, L. Marchese and C. Morterra, Structural and morphological modifications of sintering microcrystalline TiO_2: an XRD, HRTEM and FTIR study, *Applied Surface Science*, **70/71**, 200-205 (1993).

40. Y. G. Borodko, L. Ioffe, T. Halachev, P. Bosch, A. Cuan, I. N. Ivleva and Y. M. Shulga, Interaction of Pt/TiO_2 samples with H_2 and O_2: magnetic and structural properties, *Materials Chemistry and Physics*, **58**, 199-203 (1999).
41. R. J. Gonzalez, R. Zallen and H. Berger, Infrared reflectivity and lattice fundamentals in anatase TiO_2, *Physical Review B*, **55 (11)**, 7014-7017 (1997).
42. Th. E. Weirich, M. Winterer, S. Seifried, H. Hahn, H. Fuess, Rietveld analysis of electron powder diffraction data from nanocrystalline anatase, TiO_2, *Ultramicroscopy*, **81**, 263-270 (2000).
43. *JCPDS*, 21-1272 (1997).
44. J. Muscat, N. M. Harrison and G. Thornton, Effects of exchange, correlation, and numerical approximations on the computed properties of the rutile TiO2 (100) surface, *Physical Review B*, **59 (3)**, 2320-2326 (1999).
45. A. Turkoviæ, M. Ivanda, S. Popoviæ, A. Tonejc, M. Gotiæ, P. Dubèek and S. Musiæ, Comparative Raman, XRD, HREM and SAXS studies of grain sizes in nanophase TiO_2, *Journal of Molecular Structure*, **410-411**, 271-273 (1997).
46. I. Matko, M. Gaidi, J. L. Hazemann, B. Chenevier and M. Labeau, Electrical properties under polluting gas (CO) of Pt- and Pd-doped polycrystalline SnO_2 thin films: analysis of the metal aggregate size effect, *Sensors and Actuators B*, **59**, 210-215 (1999).
47. A. Cirera, A. Vilà, A. Diéguez, A. Cabot, A.Cornet and J. R. Morante, Microwave processing for the low cost, mass production of undoped and in situ catalytic doped nanosized SnO_2 gas sensor powders, *Sensors and Actuators B*, **64**, 65-69 (2000).
48. D. Mardare and P. Hones, Optical dispersion analysis of TiO_2 thin films based on variable-angle spectroscopic ellipsometry measurements, *Materials Science and Engineering B*, **68,** 42–47 (1999).
49. Y. Zhu, L. Zhang, W. Yao and L. Cao, The chemical states and properties of doped TiO_2 film photocatalyst prepared using the Sol-Gel method with $TiCl_4$ as a precursor, *Applied Surface Science*, **158,** 32–37 (2000).
50. J. Kappler, Herstellung von Halbleitergassensoren durch Sol-Gel Technologie auf Dickschicht basis, *Research. Thesis (Diplomarbeit)*, University of Tübingen, Tübingen (1997).
51. E. Cominia, G. Faglia, G. Sberveglieri, Y. X. Li, W. Wlodarski, M. K. Ghantasala, Sensitivity enhancement towards ethanol and methanol of TiO_2 films doped with Pt and Nb, *Sensors and Actuators B*, **64**, 169–174 (2000).

52. R. Rella, P. Siciliano, S. Capone, M. Epifani, L. Vasanelli and A. Licciuli, Air quality monitoring by means of sol-gel integrated tin oxide thin films, *Sensors and Actuators B*, **58**, 283-288 (1999).

53. A. Diéguez, A. Romano-Rodríguez, J. R. Morante, J. Kappler, N. Bârsan and W. Göpel, Nanoparticle engineering for gas sensor optimization: improved sol-gel fabricated nanocrystalline SnO_2 thick film gas sensor for NO_2 detection by calcination, catalytic metal introduction and grinding treatments, *Sensors and Actuators B*, **60**, 125-137 (1999).

54. G. Tournier, C. Pijolat, R. Lalauze and B. Patissier, Selective detection of CO and CH4 with gas sensors using SnO2 doped with palladium. *Sensors and Actuators B*, **26-27**, 24-28 (1995).

55. K. Suzuki, M. Ichiara and S. Takeuchi, High-resolution electron microscopy of lattice defects in TiO_2 and SnO_2, *Philosophical Magazine A*, **63**, 657-665 (1991).

56. B. Correa-Lozano, Ch. Comninellis and A. De Battisti, Physicochemical properties of SnO_2-Sb_2O_5 films prepared by spray pyrolisis technique, *Journal of the Electrochemical Society*, **143 (1)**, 203-209 (1996).

57. D. Mardare, M. Tasca, M. Delibas and G. I. Rusu, On the structural properties and optical transmittance of TiO_2 r.f. sputtered thin films, *Applied Surface Science*, **156**, 200-206 (2000).

58. G. Sberveglieri, Classical and novel techniques for the preparation of SnO_2 thin film gas sensors, *Sensors and Actuators B*, **6**, 239–247 (1992).

59. W. Göpel. In: W. Göpel, T.A. Jones, M. Kleitz, I. Lundström and T. Seiyama, Editors, Chemical and Biochemical Sensors 2, VCH, Weinheim (1991), p. 61.

60. W. Göpel, G. Reinhardt, Metal oxide sensors: New devices through tailoring interfaces on the atomic scale, *Sensors and Actuators Update* ***vol.1*****,** *H. Baltes, W. Göpel, J. Hesse, Eds.,* Weinheim (1996).

61. V. M. Jiménez, J. P. Espinós and A. R. González-Elipe, Effect of texture and annealing treatments in SnO_2 and Pd/SnO_2 gas sensor materials, *Sensors and Actuators B*, **61**, 23-32 (1999).

62. Y. Shimizu, T. Maekawa, Y. Nakamura and M. Egashira, Effects of gas diffusivity and reactivity on sensing properties of thick film SnO2 based sensors, *Sensors and Actuators B*, **46**, 163-168 (1998).

63. N. Yamazoe, Y. Kurokawa and T. Seiyama, Effects of additives on semiconductor gas sensors, *Sensors and Actuators B*, **4**, 283-289 (1983).

64. D. Kohl, The role of noble metals in the chemistry of solid-state gas sensors, *Sensors and Actuators B*, **1**, 158-165 (1990).
65. J.F. McAleer, P.T. Moseley, J.O.W. Norris, D.E. Williams and B.C. Tofield, Tin oxide gas sensors: Part 2. The role of surface additives, *Journal of the Chemical Society Faraday Trans.*, 1 **84 (2)**, 441-457 (1988).
66. J. Mizsei, How can sensitive and selective semiconductor gas sensor be made?, *Sensors and Actuators B*, **23**, 173-176 (1995).
67. Y. Shimizu, E. Kanazawa, Y. Takao and M. Egashira, Modification of H_2-sensitive breakdown voltages of SnO_2 varistors with noble metals, *Sensors and Actuators B*, **52**, 38-44 (1998).
68. N. Yamazoe, Y. Kurokawa and T. Seiyama, Effects of additives on semiconductor gas sensors, *Sensors and Actuators B*, **4**, 283-289 (1993).
69. N. Yamazoe, New approaches for improving semiconductor gas sensors, *Sensors and Actuators B*, **5**, 7-19 (1991).
70. A. R. Phani, S. Manorama and V. J. Rao, Preparation, characterization and electrical properties of SnO_2 based liquid petroleum gas sensor, *Materials Chemistry and Physics*, **58**, 101-108 (1999).
71. A. R. Phani, S. Manorama and V. J. Rao, The nature of surface behavior of tin oxide doped sensors: X-ray photoelectron spectroscopy studies before and after exposure to liquid petroleum gas, *Journal of Physics and Chemistry of Solids*, **61**, 985-993 (2000).
72. M. Gaidi, B. Chenevier and M. Labeau, Electrical properties evolution under reducing gaseous mixtures (H_2, H_2S, CO) of SnO_2 thin films doped with Pd/Pt aggregates and used as polluting gas sensors, *Sensors and Actuators B*, **62**, 43-48 (2000).
73. V. Brynzari, G. Korotchenkov and S. Dmitriev, Simulation of thin gas sensors kinetics, *Sensors and Actuators B*, **61**, 143-153 (1999).
74. O. Renault, A. V. Tadeev, G. Delabouglise and M. Labeau, Integrated solid-state gas sensors based on SnO_2 (Pd) for CO detection, *Sensors and Actuators B*, **59**, 260-264 (1999).
75. A. V. Tadeev, G. Delabouglise and M. Labeau, Influence of Pd and Pt additives on the microstructural and electrical properties of SnO_2-based sensors, *Materials Science and Engineering*, **B57**, 76-83 (1998).

76. N. Bârsan, J. R. Stetter, M. Findlay, Jr. and W. Göpel, High-Performance Gas Sensing of CO: Comparative Tests for Semiconducting (SnO_2-Based) and for Amperometric Gas Sensors, *Analytical Chemistry,* **71 (13)**, 2512-2517 (1999).
77. G. Sberveglieri (Ed.), Gas Sensors, *Kluwer Academic Publications*, The Nederlands (1992).
78. A. M. Gutiérrez, J. A. Díez de Ulzurrun, S. M. Olaizola, E. Terrón, G. García, E. Castaño and F. J. Gracia, Influence of the thin film thickness on the methane gas sensor selectivity, *Sensor 99 Proceedings*, Nürnberg, in press.
79. W. K. Choi, S. K. Song, J. S. Cho, Y. S. Yoon, D. Choi, H.-J. Jung and S. K. Koh, H_2 gas-sensing characteristics of SnO_x sensors fabricated by a reactive ion-assisted deposition with/without an activator layer, *Sensors and Actuators B*, **40**, 21 (1997).
80. D. Rosenfeld, R. Sanjinés, W.H. Schreiner and F. Lévy, Gas sensitive and selective SnO_2 thin polycrystalline films doped by ion implantation, *Sensors and Actuators B*, **15-16**, 406-409 (1993).
81. T. B. Fryberger and S. Semancik, Conductance Response of Pd/SnO_2(110) Model Gas Sensors to H_2 and O_2, *Sensors and Actuators B*, **2**, 305 (1990).
82. I. Hayakawaa, Y. Iwamotoa, K. Kikutab and S. Hiranob, Gas sensing properties of platinum dispersed-TiO_2 thin film derived from precursor, *Sensors and Actuators B*, **62**, 55–60 (2000).
83. H.P. Kim, J. Choi, H. Cheong, J. Kim and J. Kim, Sensing mechanism of SnO_2-based sensors for alcohols, *Sensors and Acuators B*, **13-14**, 511-512 (1993).
84. S.M. Olaizola, A. Cirera, A. Cornet, J. R. Morante, E. Castaño and F. J. Gracia, A Pd buried layer catalysing method to improve methane selectivity, *Sensors and Actuators B*, in press.
85. C. Xu, J. Tamaki, N. Miura and N. Yamazoe, Grain size effects on gas sensitivity of porous SnO_2-based elements, *Sensors and Actuators B*, **3** 147-155 (1991).
86. A. Cabot, J. Arbiol, J. R. Morante, U. Weimar, N. Bârsan and W. Göpel, Analysis of the noble metal catalytic additives introduced by impregnation of as obtained SnO_2 sol-gel nanocrystals for gas sensors, *Sensors and Actuators B*, **70**, 87-100 (2000).
87. L. E. Depero, L. Sangaletti, B. Allieri, E. Bontempi, A. Marino and M. Zocchi, Correlation between crystallite sizes and microstrains in TiO_2 nanopowders, *Journal of Crystal Growth*, **198/199**, 516-520 (1999).

88. M. C. Carotta, M. Ferroni, D. Gnani, V. Guidi, M. Merli, G. Martinelli, M.C. Casale and M. Notaro, Nonostructured pure and Nb-doped TiO_2 as thick film gas sensors for environmental monitoring, *Sensors and Actuators B*, **58,** 310-317 (1999).
89. A. Diéguez, A. Vilà, A. Cabot, A. Romano-Rodríguez, J. R. Morante, J. Kappler, N. Bârsan, U. Weimar and W. Göpel, Influence on the gas sensor performances of the metal chemical states introduced by impregnation of calcinated SnO_2 sol-gel nanocrsytals, *Sensors and Actuators B*, **68**, 94-99 (2000).
90. P. Albers and J. Kiwi, Highly dispersed platinum on TiO_2 obtained via autoreduction of the precursor species, *Journal of Molecular Catalysis*, **58**, 115-126 (1990).
91. K. Sekizawa, H. Widjaja, S. Maeda, Y. Ozawa and K. Eguchi, Low temperature oxidation of methane over Pd catalyst supported on metal oxides, *Catalysis Today*, **59**, 69-74 (2000).
92. P. Claus, H. Berndt, C. Mohr, J. Radnik, E.- J. Shin and M. A. Keane, Pd/MgO: Catalyst Characterization and Phenol Hydrogenation Activity, *Journal of Catalysis*, **192**, 88-97 (2000).
93. G. De, A. Licciulli, C. Massaro, A. Quirini, R. Rella, P. Siciliano and L. Vasanelli, Sol-gel derived pure and palladium activated tin oxide films for gas-sensing applications, *Sensors and Actuators B*, **55**, 134-139 (1999).
94. M. H. Madhusudhana Reddy and A. N. Chandorkar, E.Beam deposited SnO_2, Pt-SnO_2 and Pd-Sno thin films for LPG detection, *Thin Solid Films*, **349**, 260-265 (1999).
95. R.F.Wood, J.N.Leboeuf, K.R.Chen, D.B.Geohegan and A.A.Puretzky, Dynamics of plume propagation, splitting, and nanoparticle formation during pulsed-laser ablation, *Applied Surface Science*, **127–129**, 151–158 (1998).
96. P. Claus, H. Berndt, C. Mohr, J. Radnik, E.- J. Shin and M. A. Keane, Pd/MgO: Catalyst Characterization and Phenol Hydrogenation Activity, *Journal of Catalysis*, **192**, 88-97 (2000).
97. P. J. Collier, J. A. Iggo and R. Whyman, Preparation and characterization of solvent-stabilized nanoparticulate platinum and palladium and their catalytic behavior towards the enantioselective hydrogenation of ethyl pyruvate, *Journal of Molecular Catalysis A: Chemical*, **146**, 149-157 (1999).
98. R. W. Devenish, T. Goulding, B. T. Heaton and R. Whyman, Preparation, characterization and properties of Groups VIII and IB metal nanoparticles, *Journal of the Chemical Society*, *Dalton Trans.*, 673 (1996).

99. M. Andersson, E. Bakchinova, K. Jansson and M. Nygren, Preparation of nanosized palladium particles anchored onto Ln_2O_3 grains with Ln = La, Nd, Sm, Eu or Gd, *Journal of Materials Chemistry*, **9**, 265-268 (1999).

100. J. C. Kennedy III and A. K. Datye, Photothermal Heterogeneous Oxidation of Ethanol over Pt/TiO_2, *Journal of Catalysis* **179,** 375–389 (1998).

101. N. Solange de Resende, J.-G. Eon and M. Schmal, $Pt\text{-}TiO_2\text{–}\gamma\text{-}Al_2O_3$ Catalyst, I. Dispersion of Platinum on Alumina-Grafted Titanium Oxide, *Journal of Catalysis*, **183**, 6-13 (1999).

102. K. Tammeveski, T. Tenno, A. Rosental, P. Talonen, L.-S. Johansson, and L. Niinistöd, The Reduction of Oxygen on $Pt–TiO_2$ Coated Ti Electrodes in Alkaline Solution, *Journal of The Electrochemical Society*, **146(2)**, 669-676 (1999).

103. J. C. Yang, Y. C. Kim, Y. G. Shul, C. H. Shin and T. K. Lee, Characterization of photoreduced Pt/TiO_2 and decomposition of dichloroacetic acid over photoreduced Pt/TiO_2 catalysts, *Applied Surface Science*, **121/122**, 525-529 (1997).

104. G. Kokkinidis, A. Papoutsis, D. Stoychev and A. Milchev, Electroless deposition of Pt on Ti — catalytic activity for the hydrogen evolution reaction, *Journal of Electroanalytical Chemistry*, **486**, 48–55 (2000).

105. Y. Gao, S. Thevuthasan, D. E. McCready and M. Engelhard, MOCVD growth and structure of Nb- and V-doped TiO_2 films on sapphire, *Journal of Crystal Growth*, **212**, 178-190 (2000).

106. Y. Gao, In-situ IR and spectroscopic ellipsometric analysis of growth process and structural properties of $Ti_{1-x}Nb_xO_2$ thin films by metal-organic chemical vapor deposition, *Thin Solid Films*, **346**, 73-81 (1999).

107. V. A. Chaudhary, I. S. Mulla and K. Vijayamohanan, Selective hydrogen sensing properties of surface functionalized tin oxide, *Sensors and Actuators B*, **55**, 154-160 (1999).

108. J. Marien, T. Wagner, G. Duscher, A. Koch and M. Rühle, Nb on $(110)TiO_2$ (rutile):growth, structure, and chemical composition of the interface, *Surface Science*, **446**, 219-228 (2000).

109. M. Labeau, M. Vallet-Regí, V. Ragel, J. Román, J. Martínez, J. Peña, E. García, A. Varela, B. Gautheron and J. M. González-Calbet, SEM and TEM study of metallic nanoparticles dispersed on SnO_2, *Proceedings of the 9th European Conference on Electron Microscopy*, *EUREM92*, **2**, Granada, Spain, 655-656 (1992).

110. M. Labeau, B. Gautheron, F. Cellier, M. Vallet-Regi, E. García and J. M. González-Calbet, Pt nanoparticles dispersed on SnO_2 thin films: a microstructural study, *Journal of the Solid State Chemistry*, **102**, 434-439 (1993).
111. S. Matsushima, J. Tamaki, N. Miura and N Yamazoe, TEM observation of the dispersion state of Pd on SnO_2, *Chemical Letters*, 1651-1654 (1989).
112. M. Labeau, B. Gautheron, G. Delabouglise, J. Peña, V. Ragel, A. Varela, J. Román, J. Martínez, J. M. González-Calbet and M. Vallet-Regí, Synthesis, structure and gas sensitivity properties of pure and doped SnO_2, *Sensors and Actuators B*, **15-16**, 379-383 (1993).
113. R. Cavicchi, V. Sukharev and S. Semancik, Time-dependent conductance of Pd-dosed SnO_2(110), *Surface Science*, **418**, L81-L88 (1998).
114. A. Ruiz, J. Folch, J. Arbiol, A. Cirera, A. Cornet and J. R. Morante, Structural Analysis of the platinum as catalytic additive in TiO_2 gas sensitive layers, submitted to *Thin Solid Films*.
115. J. Arbiol, A. Ruiz, A. Cirera, F. Peiró, A. Cornet, J. R. Morante, A. Alimoussa and M.- J. Casanove, Analysis of Pt-Nanoparticles Embedded on Crystalline TiO_2 studied by Transmission Electron Microscopy, *MRS FALL 2000 Proceedings*, Boston (2000).
116. J. Arbiol, A. Ruiz, A. Cirera, F. Peiró, A. Cornet, J. R. Morante, A. Alimoussa and M.- J. Casanove, Platinum nanoclusters dispersion in TiO_2 nanopowders, submitted to *Journal of Materials Research*.
117. D. A. Bonnell, B. Huey and D. Carroll, In-situ measurementof electric fields at individual grain boundaries in TiO_2, *Solid State Ionics*, **75**, 35-42 (1995).
118. M. Casarin, C. Maccato and A. Vittadini, Electronic structure of Nb impurities in and on TiO_2, *Phys. Chem. Chem. Phys.*, **1**, 3793-3799 (1999).
119. J. Marien, T. Wagner, G. Duscher, A. Koch and M. Rühle, Nb on (110)TiO_2 (rutile):growth, structure, and chemical composition of the interface, *Surface Science*, **446**, 219-228 (2000).
120. T. Bredow and G. Pacchioni, A quantum-chemical study of Pd atoms and dimers supported on TiO_2(110) and their interaction with CO, *Surface Science*, **426**, 106-122 (1999).
121. S. Matsushima, Y. Teraoka, N. Miura and N. Yamazoe, Electronic interaction between metal additives and tin dioxide-based gas sensors, *Japanese Journal of Applied Physics*, **27** 1798 (1988).

122. A. R. Phani, X-ray photoelectron spectroscopy studies on Pd doped SnO_2 liquid petroleum gas sensor, *Applied Physics Letters*, **71**, 2358 (1997).
123. T. Kobayashi, M. Haruta, H. Sano and M. Nakane, A selective CO sensor using Ti-doped á-Fe_2O_3 with coprecipitated ultrafine particles of gold, *Sensors and Actuators B*, **13**, 339 (1988).
124. M. Egashira, M. Nanashima, and S. Kawsumi, *ACS Symposium Series, American Chemical Society*, Washington, DC, **309**, 71-82 (1986).
125. G.C. Bond, L.R. Molloy and M.J. Fuller, Oxidation of carbon monoxide over palladium-Tin(IV) oxide catalysts: an example of spillover catalysis, *Journal of the Chemical Society Chemical Communications*, 796-797 (1975).
126. Y. Volokitin, J. Sinzig, L. J. de Jongh, G. Schmid, M. N. Vargaftik and I. I. Moiseev, Quantum-size effects in the thermodynamic properties of metallic nanoparticles, *Nature*, **384**, 621-623 (1996).
127. J. Walter and H. Shioyama, Quasi two-dimensional palladium nanoparticles encapsulated into graphite, *Physics Letters A*, **254**, 65-71 (1999).
128. S. Bouarab, C. Demangeat, A. Mokrani and H. Dreyssé, *Physics Letters A*, **151**, 103 (1990).
129. K. Lee, Possible magnetism in small palladium clusters, *Physical Review B*, **58 (5)**, 2391-2394 (1998).
130. B. Joyce, Self-organization yields quantum-dot devices, *Vacuum Solutions*, **17**, 11-14 (2000).
131. T. Suzuki and R. Souda, The encapsulation of Pd by the supporting TiO_2 (110) surface induced by strong metal-support interactions, *Surface Science*, **448**, 33-39 (2000).
132. F. Petsy, H-P. Steinrück and T. E. Madey, Thermal stability of Pt films on TiO_2(110): evidence for encapsulation, *Surface Science*, **339**, 83-95 (1995).
133. A. Dickinson, D. James, N. Perkins, T. Cassidy and M. Bowker, The photocatalytic reforming of methanol, *Journal of Molecular Catalysis A: Chemical*, **146**, 211-221 (1999).
134. R. F. Wood, J. N. Leboeuf, D. B. Geohegan, A. A. Puretzky and K. R. Chen, Dynamics of plume propagation and splitting during pulsed-laser ablation of Si in He and Ar, *Physical Review B*, **58 (3)**, 1533-1543 (1998).
135. M. S. Tzou, B. K. Teo and W. M. H. Sachtler, Formation of Pt Particles in Y-Type Zeolites, The Influence of Coexchanged Metal Cations, *Journal of Catalysis*, **113**, 220-235 (1988).

136. A. Blažková, I. Csölleová and V. Brezová, Effect of light sources on the phenol degradation using Pt/TiO_2 photocatalysts immobilized on glass fibers, *Journal of Photochemistry and Photobiology A: Chemistry*, **113**, 251-256 (1998).
137. S. Matsushima, K. Kobayashi and M. Kohyama, Semiempirical Band Calculation of Pd-Adsorbed SnO_2 Surface, *Japanese Journal of Applied Physics*, **38**, 4993-4996 (1999).
138. Z. W. Pan, Z. R. Dai and Z. L. Wang, Nanobelts of Semiconducting Oxides, *Science*, **291**, 1947-1949 (2001).

2. Characterization Techniques and Structural Modelling

2.1 Introduction

The aim of this *Chapter* is to provide the future readers with a simple guide showing the most used analytical techniques for SGS materials characterization. In the following we briefly describe the techniques, showing their main characteristics, comparing their analytical properties and discussing the advantages or disadvantages of every technique.

In a first part, we present an overview of the most commonly used spectroscopic techniques such as X-Ray Diffraction (XRD), X-ray Photoelectron Spectroscopy (XPS), Raman Spectroscopy (Raman) and Induced Coupled Plasma (ICP). As we point out during the *Chapter*, all these techniques can give us a good general characterization of the SGS gas sensor materials. Nevertheless, they are blind in front of characterization of the metal additives morphology and distribution in these SGS systems, important parameters in order to understand the gas sensing phenomena.

The work carried out in this *Ph.D. Thesis* is mainly based in the structural analysis of the samples through *transmission electron microscopy* and complementary analytical techniques. In this way, we just tried to emphasize the procedures or applications that were innovative in our lab, establishing the basis for future works. The use of TEM related techniques allow us to analyze the nanostructural and morphological properties of the samples, such as the grain and cluster size, shape, epitaxial relations, structural phases, etc. Moreover, it is useful in order to characterize the loading distribution properties, such as metal dispersion, nanocluster size distribution, superficial metal density, etc.

In this way, in the second part of the *Chapter* we extend on the description of those Transmission Electron Microscopy related techniques: such as conventional Transmission Electron Microscopy (TEM), High Resolution Transmission Electron Microscopy (HRTEM), Selected Area

Electron Diffraction (SAED) and Electron Dispersive X-Ray Spectroscopy (EDS). These techniques are intended to be a powerful tool in order to provide a nanostructural characterization of the SGS materials. The Digital Image Processing (DIP) and Computer Image Simulation (CIS) are also presented as indispensable complementary tools to HRTEM as we will also see in the next *Chapters*. The part related to convolution and median filters is described in more detail because the software used in order to process the images has been developed in our department, and specifically for the use and help of this Ph.D. work.

Finally, at the end of the *Chapter*, we include the characteristics of the equipment and software applications used along the work.

2.2 General Characterization Techniques

The main part of the works found in literature devoted to analyze the SGS materials uses a set of common techniques. These techniques are mainly used in order to obtain a general characterization of the samples: such as chemical composition and structure. At the end of every *Section* we will show some interesting bibliography where further explanations and examples of every technique are given.

2.2.1 X-Ray Diffraction

This technique analyzes the interaction of X-rays with the crystalline matter through their diffraction. The X-ray beam diffracts when crossing the crystal and produces beams at different angles depending on the X-ray wavelength, the crystal orientation and the structure of the crystal. The common X-rays wavelengths used are Mo K_α at 0.71359 Å and the Cu K_α at 1.54056 Å.

X-ray spectra allow us to identify and analyze any crystalline matter. The degree of crystallinity conditions the quality of the result obtained. The application of XRD technique to polycrystalline materials such as SGS nanopowders gives us a set of peaks with angular separations satisfying the Bragg's law. These peaks can be indexed and related to a determinate crystalline structure using some patron tables as the well-known *JCPDS*, published by the American Society for Testing and Materials.

The advantages that this analytical technique brings, are an easy quantification of the crystalline phases that compose the samples, and the possibility of evaluating the mean grain size of the nanopowders in polycrystalline samples. However, in order to obtain accurate results in this quantification, we have to be sure of the sample structure, and some initial patron models are needed. This technique has been widely used for the

identification of material structural phase [1, 2]. In this way, Turkoviæet al. [3], carried out their TiO_2 nanophase sample structural characterization by means of this technique, identifying a mixture of anatase and brookite in their pre-annealed material and showing the feasibility of the technique in this field. Moreover, an accurate analysis of phase transitions in SGS materials can be also carried out when analyzing samples treated at different annealing temperatures or even performing in-situ XRD analysis. As Depero et al. [4], achieved in their studies about anatase to rutile phase transitions when metal additives had been loaded to the samples.

Further readings about the XRD technique principles can be found elsewhere [5, 6, 7].

2.2.2 X-ray Photoelectron Spectroscopy

This is maybe the quantitative surface analysis technique most sensitive to the chemical structure.

XPS is based on the analysis of the electrons emitted by a solid in vacuum after being irradiated with monoenergetic soft X-rays (Mg K_α at 1253.6 eV and Al K_α are commonly used). The application of this technique allows us to identify, determine and even quantify the concentration of the elements on the surface and moreover, to identify the chemical states from an exact measurement of the peak positions and separations. As we have seen, the advantages of XPS are notorious.

Nevertheless, there are some disadvantages that we should take into account. Firstly and due to the reduced mean free path of the electrons in a solid, the detected electrons will mainly come from the first atomic monolayers (1-5 nm). Therefore, XPS will be perfect for chemical surface analysis, but not so useful in order to obtain the chemical composition of materials bulk. Secondly, the technique induces some damage to the sample, overheating the analyzed zone and destroying the local crystal structure.

There are several works in literature devoted to the chemical and electronic analysis of materials surface, carried out by means of XPS [8, 9, 10]. In this way, Atashbar and co-workers [11], analyzed the changes in the

Ti surface bonding when introducing Nb to their TiO_2 nanophase material. Or in our recent works [12], where we measured the surface metal concentration of Pd and Pt /SnO_2 loaded samples.

Further readings about the XPS technique principles can be found elsewhere [13, 14].

2.2.3 Raman Spectroscopy

Raman Spectroscopy is based in the diffusion processes given by the electronic polarization caused by ultraviolet or visible light. Raman gives information at molecular level allowing the vibrational and rotational analysis of chemical species. Briefly, the radiation interacts with the molecular vibrational energy levels due to the light scattering phenomena, in which the electromagnetic radiation interacts with a pulsating polarizable electron cloud.

As a consequence of the diffusion effect, this technique presents several advantages. On one hand, there is no needing of any sample preparation making easier its implementation. Moreover, it provides a non-destructive and quantitative microanalysis of structures and electronic properties.

As well as XRD, this technique has been widely used for the identification of material structural phase, as in those works carried out by Tompsett et al. [15] or R. J. González [16], and moreover for the analysis of phase transitions. But it can also be used to determine when the catalytic species are placed inside the semiconductor lattice, by analyzing the Raman peaks shift, as carried out by Cabot et al. [17] in their work about Pd-Pt/SnO_2 systems.

The principles of this spectroscopic technique are widely reported elsewhere [18, 19].

2.2.4 Induced Coupled Plasma

ICP (Inductively Coupled Plasma) spectrometry is the most widely used multi-element technique. It provides fast, reliable and accurate analysis

with high sensitivity [20]. This analytical technique uses an inductively coupled plasma source to dissociate the sample into its constituent atoms or ions, exciting them to a level where they emit light of a characteristic wavelength. A detector measures the intensity of the emitted light, and calculates the concentration of that particular element in the sample.

When undergoing ICP analysis, the sample experiences temperatures as high as 10,000° C, where even the most refractory elements are atomized with high efficiency. As a result, detection limits for these elements can be typically at the 1-10 parts-per-billion level [21].

With respect to the ICP analysis, the knowledge of the analysis procedure will be useful for the results presented in this work. Thus, in order to analyze the sample, we will need to introduce the sample in a solution. The dissolution process is made in three sequential chemical steps:

1- The sample is immersed in a solution of aqua regia ($HCl:HNO_3$ 3:1) in order to solubilize all the catalyst species present on the surface. In this process we also solubilize possible tin or titanium species that doesn't come from the metal oxides. With the first step, we will measure the additive species that are not inside metal oxide support, such as additives forming nanoclusters on surface, macro-agglomerated metal particles and ultradispersed metal surface atoms.
2- An alkali fusion process with Na_2O_2 and Na_2CO_3 that solubilizes metal oxides. In this step we will obtain the total quantity of semiconductor material acting as support.
3- If any solid remains after the second step, it is again solubilized in a solution of aqua regia. In this step we would solubilize the catalytic metal that was placed inside metal oxide.

Following these three steps, we can measure accurately our specimen composition, and furthermore, we can find where the loaded catalytic was placed (in or outside the semiconductor material).

This technique has been widely used in our recent works in order to determine the global chemical composition of the samples [22, 23].

Further descriptions about the technique, principles and procedure can be found elsewhere [24].

2.2.5 Main Disadvantages of the General Characterization Techniques

It has been shown that the analysis performed with the techniques described in the former *Sections* can give us excellent results when analyzing the general chemical composition and structure of materials. However, all these techniques have a common characteristic, although the results given are precise, they usually integrate the information coming from a wide area, containing a high number of particles and grains. In our case, the use of these techniques will be a good starting point, nevertheless, the aim of this work is to go further, and analyze the material at the atomic scale, obtaining the nanoscopic features, of composition and structure. This is the reason, why we have centered our studies in the use of nanoscopic techniques such as TEM related techniques, which offer a great precise control of the specific point studied. These TEM related techniques will be introduced in the following *Section*.

2.3 Transmission Electron Microscopy

Transmission Electron Microscopy (TEM) has been the central analysis technique used in our work. A great part of the work developed consists in the evaluation of the additive dispersion in the studied semiconductor oxides. Basic results about semiconductor nanoparticles size have been obtained using conventional TEM under bright-field conditions [25]. Under these conditions, we could also observe the macro-agglomerated metals, with cluster sizes as big as the semiconductor nanoparticles size. In order to study material structure and morphology we have used High Resolution Electron Microscopy (HRTEM). This technique allows us to obtain images of the atomic structure of the materials studied. At the present time, modern electron microscopy can give resolutions of less than 2 Å, which is sufficient in order to characterize cluster cores of the heavier transition metals at atomic resolution [26]. In this way, we could study the metal nanoclusters morphology. However, HRTEM have a disadvantage: since the energy of the electron beam can be as much as 300 keV, the particles are heated up rapidly and rearrangement and coalescence processes may result. This a priori non-desired phenomenon has been used in the in-situ reduction processes carried out in chapter 5 for the study of ultradispersed additives.

2.3.1 Sample and Grid preparation

In comparison with other materials, powder samples are the easiest to prepare. The greatest advantage is that grain size is normally thin enough to let the electrons pass through material, and no thinning is needed. There are two important parameters that we should improve in order to obtain good images of our nanoparticles. On one hand, we will have to assure a good dispersion of the nanopowders, avoiding their agglomeration. And on the

other hand, it will be interesting to obtain grid membranes as thin as possible to improve TEM image.

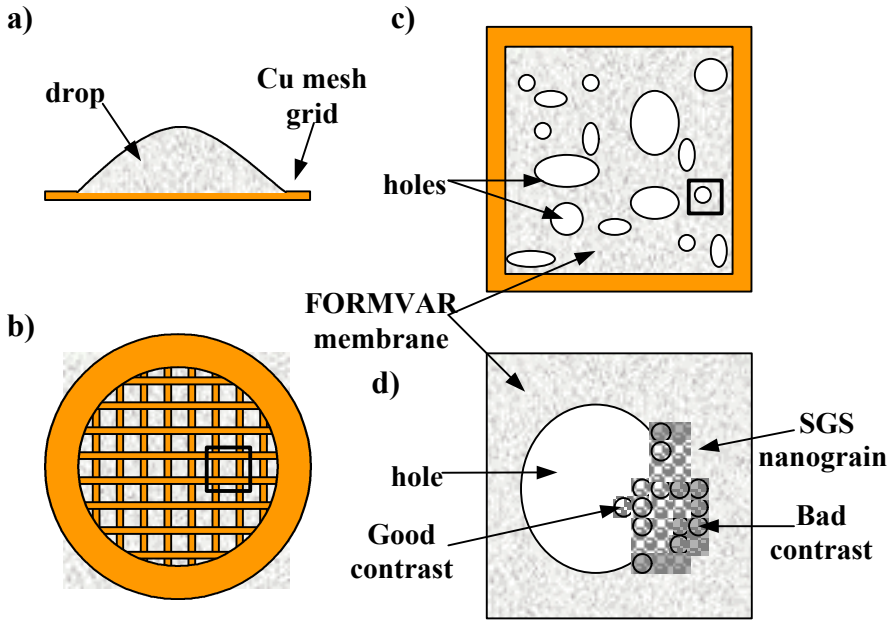

Figure 2.1. a) A drop containing the mixture of ethanol and our SGS material is deposited on a Cu mesh grid. **b)** After ethanol evaporation, our material remains in the FORMVAR membrane with holes. **c)** Magnified detail of the membrane d) SGS nanopowders suspended on a hole will display good constrast HRTEM images.

Good dispersion results of nanograins were obtained as follows:

1- Mixing of approximately 1 part of powder with 100-500 parts of high purity ethanol. No influence of ethanol over structural and morphological characteristics of the samples has been observed.[♣]

[♣] Some other solvents were used with sample nanopowders. Acid and basic liquid species were tested in order to obtain good particle dispersion, but we found that low or high pH affected the sample and the FORMVAR membrane attacking chemically their structure. Ethanol was selected for its, a priori, innocuous properties over sample and grid membrane.

2- Ultrasonic dispersion of the mixture. This process let a dispersion of agglomerated material.
3- Deposition of a single drop of the dispersed material mixture on a FORMVAR carbonated film with holes placed on a ~ 400 mesh grid.
4- Evaporation of ethanol from the grid in a dry environment.

As it is well known, the crystalline nanoparticle's contrast tends to get lost because of the noise generated in the amorphous films [27]. This noise will increase when the thickness of the membrane is thicker. In order to avoid this problem, we prepared our FORMVAR membranes with holes. Nanoparticles placed on the border of a hole can be imaged easier, obtaining better contrast for HRTEM micrographs. In *figure 2.1*, we show a scheme of the deposition process of our SGS material on the grid.

2.3.2 Bright field TEM

As explained by other authors [27], bright field images can provide images with a good contrast. This property was useful to measure the particle and cluster sizes. In bright field conditions, we select the direct electron beam (not scattered) from the diffraction pattern. The direct beam is selected with the objective aperture. If we form the image with a wide objective aperture the contrast of the image will be poor because many beams contribute to the image. All the possible aspects concerning this technique are extensively reported in literature [25, 28]. Furthermore, an extended summary of TEM conventional analysis applied to nanopowders study was made in Diéguez Ph.D. Thesis [29], thus we will not go into further explanations here.

2.3.3 HRTEM and Nanostructural Analysis

As it has been widely demonstrated in literature, HRTEM is a powerful tool for the morphological and structural analysis of crystalline samples and specially when these samples are mainly composed of nanometric structures, as in the case of metallic nanoclusters on metal oxide support [30, 31, 32]. To extract the maximum information from HRTEM images and to obtain a perfect understanding, we have processed the micrographs digitally and performed computer simulations.

In the following, we will introduce the basic theory of image formation. This theory has been extracted from a M. José-Yacamán et al. recent work [33]. This basic theory will be useful for the reader in order to understand the image processing techniques explained later in this chapter:

2.3.3.1 Basic theory of image formation

The image observed on the screen or on the micrograph is the result of two basic processes:

- Firstly, the interaction of the electron beam with the sample. The electron beam, represented by an incoming wave function (y_i) interacts with the sample and as a result of its interaction with the atomic potential becomes (y_o), the outgoing wave function.
- Secondly, the interaction of the outgoing wave function with the microscope. Although, ideally the microscope should do nothing but produce an enlarged image of the potential distribution in the sample; in practice, microscopes are aberrated optical systems in which defocus, astigmatism, spherical aberration and chromatic aberration are present.

Interaction of the electron beam with the sample

First of all we will introduce some basic terminology. In the following, the potential seen by the electrons will be represented by the function:

$$V(\vec{r}) = V(x, y, z) \tag{2.1}$$

The interaction of the electron beam with the sample can be described by dividing the sample into several slices, each of thickness Δz (here z is the coordinate in the direction of the incoming electron beam). The potential is considered as concentrated on the exit surface of each slice so the motion of the beam through the slice actually consists of two stages:

- Propagation from the entrance surface of the slice to the exit surface. Here the potential is considered to be zero (free particle propagation).
- Transmission by the potential (assumed to be concentrated at the exit surface).

So, in a given slice, extended from z to $z + \Delta z$ the incoming wave function $y_i(x,y,z)$ first becomes:

$$y_i^-(x, y, z + \Delta z) = y_i(x, y, z) * P_{\Delta z}(x, y) \tag{2.2}$$

where * denotes the convolution product and the function,

$$P_{\Delta z}(x, y) = \frac{-ie^{2pic^2} e^{ip(x^2+y^2)/l\Delta z}}{lz} \tag{2.3}$$

is the free propagator as described in elementary textbooks on quantum mechanics. The various constants have their usual meaning; l is the electron wavelength, $c = 1/l$. The "$^-$" in y_i^- is used to denote the wave function before transmission by the atomic potential.

The wave function $y_o(x,y,z + Dz)$ exiting the slice is given by

$$y_o(x, y, z + \Delta z) = y_i^-(x, y, z + \Delta z) e^{-is\,Vp(x,y)} \tag{2.4}$$

where s is the so-called interaction constant defined as,

$$s = \frac{p}{lE} \tag{2.5}$$

with E being the energy of the electrons. The function $V_p(x,y)$ is the projected potential of the slice,

$$V_p(x, y) = \int_z^{z+\Delta z} V(x, y, z) dz \tag{2.6}$$

Putting the various pieces together

$$y_o(x,y,z+\Delta z) = y_i(x,y,z) * P_{\Delta z}(x,y) e^{-isVp(x,y)} \quad (2.7)$$

Once this is done for the first slice $y_o(x,y,z + Dz)$ is considered as the input wave function for the second slice

$$y_i(x,y,z + Dz) = y_o(x,y,z + Dz) \quad (2.8)$$

and the procedure is repeated for all the slices.

Weak phase object approximation

Frequently the potential term in $e^{-isVp(x,y)}$ is sufficiently small that the so-called weak phase object approximation

$$e^{-isVp(x,y)} \approx 1 - isV_p(x,y) \quad (2.9)$$

can be made.

Interaction of the electron beam with the microscope

There is a relationship between the wave function y (x,y) leaving the sample and the wave function after the various lenses, mainly the objective lens. This relationship is expressed in reciprocal space (i.e. in terms of the Fourier transform of y (x,y)) as

$$\hat{\Psi}_m(u,v) = \hat{\Psi}(u,v) T(u,v) \quad (2.10)$$

where $\hat{\Psi}_m$ represents the Fourier transform of the wave function after the lenses and $\hat{\Psi}$ represents the Fourier transform of the wave function before the lenses. The variables u and v are spatial frequencies and T (u,v) is a function that describes the effect of the microscope. It is called the contrast transfer function and it is given by:

$$T(u,v) = A(u,v) e^{ic(u,v)} \quad (2.11)$$

where

$$c(u,v) = p\,l\left[D|(u,v)|^2 - \frac{1}{2} C_s\, l^2 |(u,v)|^4 \right] \quad (2.12)$$

here D is the defocus and C_s is the spherical aberration coefficient.

Weak phase object contrast

Under the weak phase object approximation, when the transfer by the microscope is taken into account, the wave function becomes

$$\hat{\Psi}_m(u,v) = \hat{\Psi}(u,v)T(u,v) = \left(d(u,v) - is\hat{V}_p(u,v)\right)A(u,v)e^{ix(u,v)} \qquad (2.13)$$

The intensity distribution at the image *I* can be calculated as $I = |y(x,y)|^2$ or better, in Fourier space as

$$\hat{I}(u,v) = \hat{\Psi}_m(u,v) * \hat{\Psi}_m^*(-u,-v) \qquad (2.14)$$

It is more convenient to work not with *I* directly but instead with the contrast

$$c(x,y) = I(x,y) - 1 \qquad (2.15)$$

so from the previous equations

$$\hat{c}(u,v) = -2is\hat{V}_p(u,v)A(u,v)sin(c) \qquad (2.16)$$

This is probably the most important and useful equation when it comes to understand the relationship between what ones sees and the structure of the sample. The part $sin(c(u,v))$ tells us how well the various spatial frequencies are transferred by the microscope. In the so-called Scherzer defocus,

$$c = 0 \Rightarrow D = \sqrt{C_s l} \qquad (2.17)$$

and the transfer is close to one for a broad range of frequencies. In this widely used defocus setting, atoms appear as dark spots (*figure 2.2*).

Figure 2.2. Simulated image of a 147-atoms cuboctahedral nanoparticle in the Scherzer defocus. Notice that atoms appear as dark spots. The particle is imaged in <011> direction. It was obtained under 300 kV and C_s = 1.2 nm conditions**.**

2.3.3.2 Digital Image Processing Basis

Several techniques for digital image processing (DIP) of HRTEM micrographs are pointed out in literature [33, 34, 35, 36]. Most of those techniques relevant to the structural study of nanoparticles are based in one way or another on a form of filtering. These filters can be applied to the image frequency space (after a Digital Fourier Transform) or directly to the image using a simple convolution. The use of filters will enhance the particle or material structure and will decrease the noise level in our images. In *figure 2.3*, we schematically show the basic steps followed for image processing.

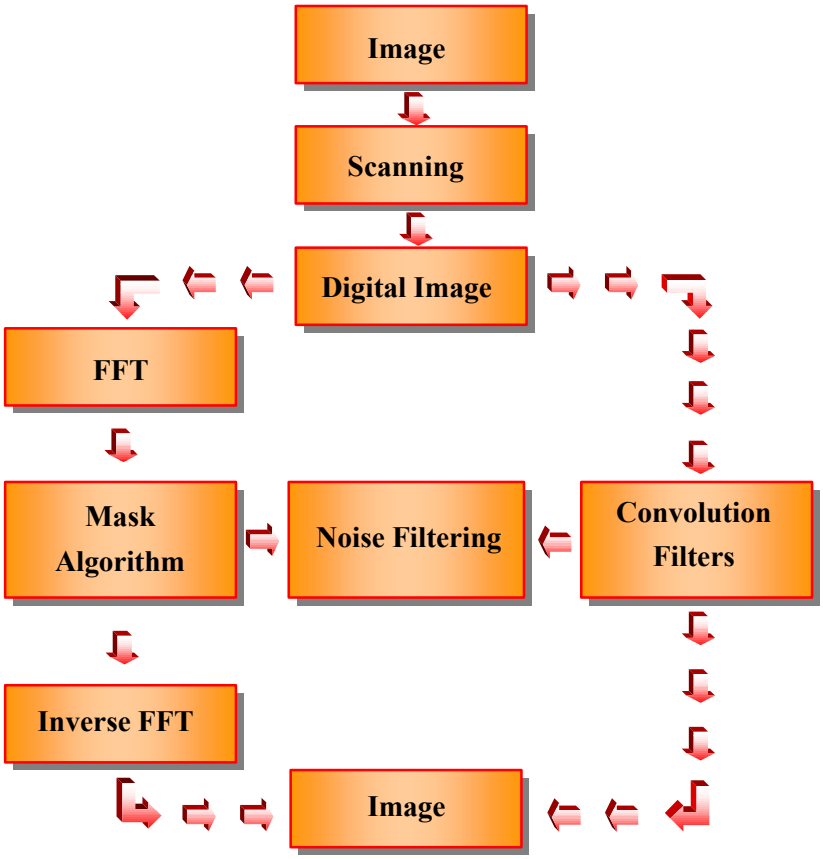

Figure 2.3. Schematic representation of the steps involved in image processing.

Digital Fourier Transform Mask Filters

If the density in a micrograph is given by a non-negative function $I(x,y)$ (or its discrete analogue), its Fourier transform is given by

$$\hat{I}(u,v) = \int_{-\infty}^{\infty} I(x,y) \cdot e^{-2pi(ux+vy)} dxdy \qquad (2.18)$$

and can be computed numerically by sampling I and using Fast Fourier Transform (FFT) techniques. Although the most common form of filtering involves a mask, that is a function S that has as values

$$S(u,v) = \begin{cases} 1 for\ (u,v) \in R \\ 0 for (u,v) \notin R \end{cases} \quad R \text{ (radius of the selected area)} \qquad (2.19)$$

,many other filtering functions can be used. There are masks that obstruct some specific spatial frequencies (a sort of digital dark field). Another frequent case is that in which the highest spatial frequencies (those associated with noise) are removed. The third case of masks includes the ones that select specific spatial frequencies, and obstruct the rest. Other algorithms include contrast speaking, histogram expansion and several other.

The process of filtering is accomplished by multiplying first $I(u,v)$ by $S(u,v)$ and then transforming back by inverse Fourier transform (inverse FFT), so the filtered image $I'(x,y)$ is given by

$$I'(x,y) = F^{-1}\left[\hat{I}(u,v) S(u,v)\right] \qquad (2.20)$$

where F^{-1} stands for the inverse FFT.

In practical terms the processing involves several steps:

- The electron micrograph is digitized, i.e. it is sampled and the values of the density of the micrograph are stored in a matrix $I_{i,j}$ where the indices i and j run from 1 to the number of samples in each direction.
- The digitized image is Fourier transformed using the discrete version of the Fourier transform

$$\hat{I}(i,j) = \sum_{h,k} I_{i,j} e^{-2pi(hi+kj)} \qquad (2.21)$$

and taking advantage of the so-called FFT algorithms.

- In this point several masks can be applied to our Fourier Transformed image.
- And in a final step we apply again the FFT over the filtered signal and obtain an image, which is cleaner than the original image. It should be always considered that image processing can improve the signal to noise ratio in an image. The mask mainly used in our work will be the one that selects specific spatial frequencies, and obstruct the rest. As shown in *figure 2.4*, this mask process give us excellent results for noise filtering and allow us to select and enhance the family of planes we prefer.

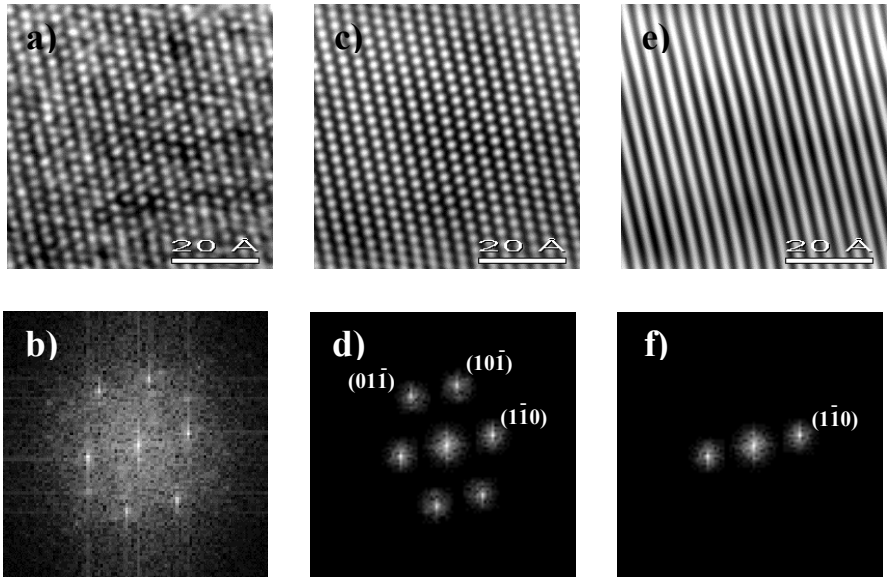

Figure 2.4. a) HRTEM micrograph of a TiO_2 nanoparticle region. **b)** FFT of the image showed in **a)**. Measuring spot distance and angles in the frequency space we found that the structure imaged corresponded to rutile stable phase. **c)** Filtered noise image. **d)** Selected frequencies used in the mask filtering for figure **c)**. We selected those frequencies corresponding to family planes (01-1), (10-1) and (1-10). **e)** Filtered image showing one specific family planes. **f)** Frequencies selected in this case correspond to (1-10) planes.

It should be stressed that the Fourier transform of a micrograph is similar in many ways to a direct diffraction pattern. In normal microscopy the diffraction pattern is basically the Fourier transform of the atomic

potential in the sample, whereas the transform of the micrograph is essentially the transform of the modulus of the wave function leaving the sample and the microscope as described above. The transform of the micrographs carries crystallographic information similar to that of the diffraction patterns. In other words the distances and angles between spots in a FT can be used in the same way as a regular diffraction pattern to find out the orientation of a determinate material [33].

In the study of nanoclusters or nanoparticles in real catalysts the support plays a very important role. The most common substrates, TiO_2, SnO_2 and graphite are crystalline at the nanoscale and therefore scatter the electrons coming out of the metal particle when this is imaged in planar view. Even if the substrate is amorphous it reduces the intensity of signal from the particles. A crucial point is the orientation relationship between the particle and the substrate. It is always desirable to orient the electron beam in such a way that the particle is strongly diffracting and the substrate is not. This produces the optimum conditions for particle imaging.

When we performed the FFT of a metal nanoparticle in planar view, it showed the spots corresponding to the particle, which appeared well defined plus the background spots due to the support. Then, we applied a mask to the spots of the particle. The spots could be identified by indexing them in the same way as we index the spots of a diffraction pattern. By Fourier transform again, we obtained an image corresponding to the "clean" particle without support information, as shown in *figure 2.5*. However, we have to be careful when we apply the masks to FFT images. If we consider a noisy image, and we apply a mask in a region where there is not a real spot, the image corresponding to the inverse of the FFT will show a false family of crystallographic planes. These false planes will be created as a periodic repetition of the masked frequency selected in the FFT image.

The mask filters in the Fourier transform of our images were carried out using commercial software programs, as it will be specified at the end of this chapter.

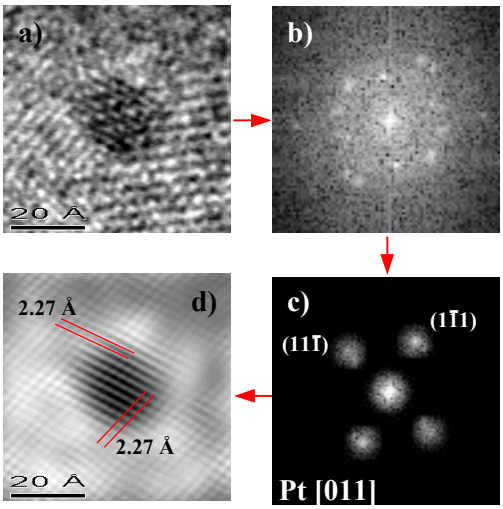

Figure 2.5. HRTEM micrograph showing a Pt nanoparticle laying on TiO_2 nanograin surface **(a)**. Digital Mask filtering on the corresponding FFT **(b)**, provided us the clean image of the particle **(d)** after we substracted the TiO_2 support information. The masking frequencies selected are also shown **(c)**.

In order to interpret HRTEM images, software programs such as *EJEZ* [1] or *Carine 3.1* [2] were of great importance. These software programs provided us the information about the possible crystallographic orientations (zone axis) of a known crystalline structure. Comparison between crystallographic data obtained from these applications with that found experimentally from HRTEM micrographies after DIP, allowed us to establish the structural phase and orientation of the material analyzed.

Convolution Filters

A somewhat more general form of processing involves a convolution with some filtering function *S*, in this case the filtered image *I'* is related to the unfiltered image *I* by means of

$$I' = I * S \qquad (2.22)$$

[1] This software was developed integrally in the Departamento de Ciencia de los Materiales e Ingeniería Metalúrgica y Química Inorgánica of Universidad de Cádiz (UCA).

[2] Commercial Software

This kind of filters can be directly applied to the previous digitized image and doesn't need the previous step of the spatial frequency transformation. These filters are versatile and have multiple possibilities. In the following we will show the most usual filters used and we will explain their properties. The software used in order to process images with convolution filters was homemade, and specifically developed for the use and help in the nanoparticles study. In this way, we created *Filtre*, a simple program that can convolute 3x3 filter matrix with the image loaded. The C code of the program created won't be given in this work due to its length. In the present we will just point out some of the applications that the *Filter* software allowed us to perform.

Depending on the values and disposition of the 3x3 matrix data elements, we obtained different filtering results. We obtained the digital convolution from the pondered product of the filter matrix with the neighbours of every image matrix pixel [37, 38, 39, 40]. To avoid the problems related with borders, the image has been considered periodical.

Filters used were 3x3, in order to decrease the calculus time. If we wanted to enhance the filtering, we wouldn't need to apply a higher dimension filter matrix, because by applying the 3x3 filter twice or more times, we would obtain the same quality results.

The most general convolution filter is the so-called *Average* filter (*A*). The 3x3 matrix used is shown in *expression 2.23*,

$$A = \begin{pmatrix} 1 & 1 & 1 \\ 1 & 1 & 1 \\ 1 & 1 & 1 \end{pmatrix} \qquad (2.23)$$

This filter calculates the average value of the surrounding neighbours of a determinate pixel, and substitutes its value with the mean value calculated. This effect is obtained after convoluting the image with the 3x3 matrix showed in *expression 2.23*. The result is a non-pondered average of pixel surroundings, and this is the value that will substitute the central data point. If we give a major weight to the central pixel of the 3x3 matrix, the smoothing effect obtained will be less abrupt.

In *figure 2.6*, we show the results obtained after convolution filter application on a TiO_2 rutile structure image.

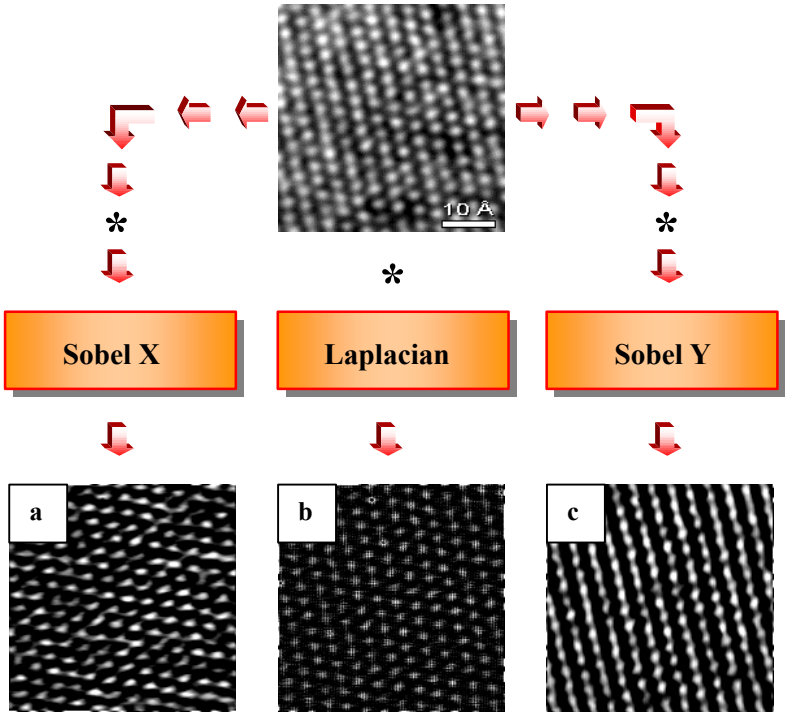

Figure 2.6. The top image corresponds to a TiO_2 rutile structure obtained by HRTEM. Three different convolution filters were applied to the original image obtaining the observed results. **a)** Sobel X, **b)** Laplacian and **c)** Sobel Y. The simbol * means that a convolution product was carried out.

The filters applied in the former case have matrix values as shown in the following expressions,

$$Gx = \begin{pmatrix} -1 & -2 & -1 \\ 0 & 0 & 0 \\ 1 & 2 & 1 \end{pmatrix} \quad (2.24), \qquad Gy = \begin{pmatrix} -1 & 0 & 1 \\ -2 & 0 & 2 \\ -1 & 0 & 1 \end{pmatrix} \quad (2.25)$$

$$Lap = \begin{pmatrix} 0 & -1 & 0 \\ -1 & 4 & -1 \\ 0 & -1 & 0 \end{pmatrix} \quad (2.26)$$

The first (2.24) and second filters (2.25) correspond to the so-called *Sobel Gx* and *Gy* directional filters. The result of applying this kind of filters

to the image is similar to a directional derivative in *x* and *y* in every image pixel, respectively. The resultant image will be the gradient of the original, enhancing lines (planes) in x or y direction respectively. Notice that the value of the central element of the matrix is related to the specific weight that we apply to a determinate pixel of the image and the rest of the matrix data elements are related with the specific weights that we apply to its first neighbours.

The third case, *expression 2.26*, correspond to a *Laplacian* filter, equivalent to a second order derivative over image matrix. *Laplacian* filters present some advantages with respect to first order gradient filters (*Sobel*) when we work with images that have poorly enhanced intensity. With this filter we obtain an enhancement on image pixels in both x and y directions.

Other examples of 3x3 convolution filters are the *directional* filters, which enhance the lines placed in a determinate direction. Enhancement is obtained for lines (planes) placed in the horizontal, *E-W* (East-West) filter (2.27), in the vertical, *N-S* (North-South) filter (2.28), and in both diagonals of the image, *NE-SW* (north-east south-west) filter (2.29) and *NW-SE* (north-west south-east) filter (2.30). Corresponding 3x3 matrix are shown below,

$$E\text{-}W = \begin{pmatrix} -1 & -1 & -1 \\ 2 & 2 & 2 \\ -1 & -1 & -1 \end{pmatrix} \quad (2.27), \qquad N\text{-}S = \begin{pmatrix} -1 & 2 & -1 \\ -1 & 2 & -1 \\ -1 & 2 & -1 \end{pmatrix} \quad (2.28)$$

$$NE\text{-}SW = \begin{pmatrix} -1 & -1 & 2 \\ -1 & 2 & -1 \\ 2 & -1 & -1 \end{pmatrix} \quad (2.29), \qquad NW\text{-}SE = \begin{pmatrix} 2 & -1 & -1 \\ -1 & 2 & -1 \\ -1 & -1 & 2 \end{pmatrix} \quad (2.30)$$

Although the possibilities of creating 3x3 matrix filters are huge, we only wanted to point out the most interesting ones for our HRTEM image processing.

Median Filter

The last filter implemented in our program was the so-called *Median* filter. This is a simple filter that give excellent results in order to neutralize the noise introduced in our digital images. The subroutine that composes this filter searches for the 8 first neighbours of every digital image pixel. Once it

has localized the neighbours' values, it puts into order the data from higher to lower values, using the bubble method [40], and it substitutes the central pixel value by the fifth data value of its ordered list. All those data values that are too high or to low in comparison with the neighbours will be suppressed. Using this subroutine we can substantially reduce the noise present in the sample image, as shown in *figure 2.7*, where *Median* filter was applied to a TiO_2 rutile structure image several times. We observe that white points corresponding to atom columns acquire circular shape after filter application, and image noise is reduced. The image has also been considered periodic in order to avoid border effects.

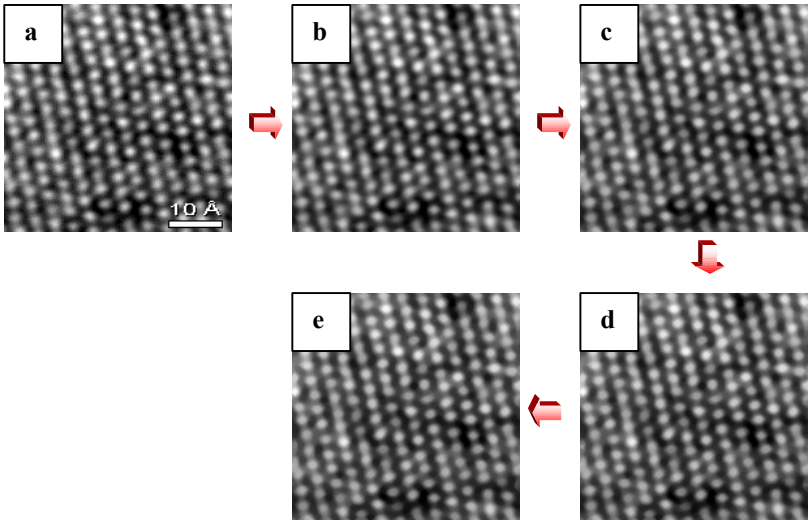

Figure 2.7. We show a sequence of images where *Median* filter was applied several times. **a)** Original TiO_2 rutile structure image, **b)** *Median* filter has been applied once, **c)** 3 applications, **d)** 5 applications and finaly **e)** 8 applications. In the last sample atom columns show quasi perfect circle shapes and noise was removed.

The filters mentioned before have been applied to some of the TEM and HRTEM micrograph images shown in this Ph.D. Thesis in order to improve its quality and facilitate its analysis. However, in the following *Chapters*, we will omit any mention to this step of image analysis for the purpose of clarity when presenting our results.

2.3.3.3 Computer Image Simulation

High Resolution Electron Microscope images are not trivially interpretable as images of atoms or columns of atoms, because of the nature of the radiation and the imaging system that are used. The imaging system is characterized by a transfer function modifying the amplitude and the phase of the Fourier components of the wave function to be imaged. Interpretation of these HRTEM images has, on occasion, been a subject of controversy because a given crystal can produce a variety of images, depending on parameters such as the objective aperture used, the focus setting (defocus) of the objective lens and crystal thickness. The ability to produce calculated images of a given (or trial) structure makes it possible to resolve such controversies [41]. As a result, the simulation of HRTEM images is a tool that may achieve a high level of accuracy when we use it to interpret the experimental images obtained [42, 43, 44, 45].

In the present work, computer image simulation (CIS) has been widely used. This technique allowed us to interpret easily the results obtained by HRTEM. Experimental images were compared with simulated ones, computed by a 'multislice' method for a set of model structures along various axes of observation.

Multislice Method

In the multislice method, the crystal is sliced perpendicular or nearly perpendicular to the direction of the observation and the potential within each slice is projected onto a plane, in order to form a phase grating. The incoming wave is then modified by successive phase object functions (POF) and propagated in-between them. Because the propagation extends over less than a nanometer, the Fresnel diffraction approximation is valid and consequently the modified wave function at the entrance of the next phase object or "slice" is the convolution of the exit wave function with a Fresnel propagator (FRE). At the end of computer calculus we obtain the simulated image of the crystalline structure selected.

Multislice simulation will be mainly used to interpret results obtained in chapter 4, where the presence of small nanostructures on semiconductors particle surface needed further study. These multislice programs sometimes require complex supercell models as input data [46]. Each supercell contains all the atomic positions of the structure under study. The simulated images were obtained using the *EMS* software package, developed by Prof. P. A. Stadelmann [42, 43, 44, 45], installed in a *Silicon Graphics* workstation *Indy R5000*.

Our supercell models have been divided into slices using the program *RODAJAS* developed in Universidad de Cádiz [47]. This program can divide every supercell in an adequate number of slices with a thickness lower than 0.2 nm and less than 2000 atomic positions.

In the following, we will describe the supercell models that will be used in our work.

Model Structures and its observation

Around 35 years ago, electron diffraction and microscopy both revealed that for various materials, small aggregates of atoms exhibit complex structures instead of being perfect monocrystals. In particular, works on the early stage of epitaxial growth of gold on sodium chloride, on silver and on mica, but also studies of Au, Ag, Ni, Pd and Co particles, have shown the existence of unexpected {111} reflections and of triangular or *butterfly*-like contrasts in bright or dark field images [48]. The metallic additives studied in chapters 4 and 5 (Pt and Pd, respectively) belong to a class of molecular metal clusters in which the metal cores are members of a series of 'magic-number' clusters obtained by surrounding an atom by successive shells of atoms of its kind [26, 49]. In the case of close packed cubic (fcc) metal clusters, a simple model to consider is a super-cell of the bulk lattice. From total free energy considerations, it appears that preferred shapes for such particles are closed-shell cuboctahedra obtained through (111) faceting of a basic fcc cube [50, 51]. Cuboctahedral packing is a way of packing equal-size spheres together so that they take the least space and

have the most structural strength. A cuboctahedron (or cube-octahedron) is a 14-sided solid made from a cube by cutting off each of the corners of the cube to make an equilateral triangle. The resulting cuboctahedron has six sides that are squares (left over from the surfaces of the original cube) and eight sides that are triangles (one made from each corner of the original cube) [52]. The (magic) number of atoms per particle obtained in this way increases as 13, 55, 147, 309, 561 and so on, corresponding to one-, two-, three-, four- and five-shell clusters (*Figure 2.8*). In *figure 2.9* we show the schema of a 309-atom cuboctahedral Pt nanocluster imaged in three different zone axis directions: [111], [001] and [011].

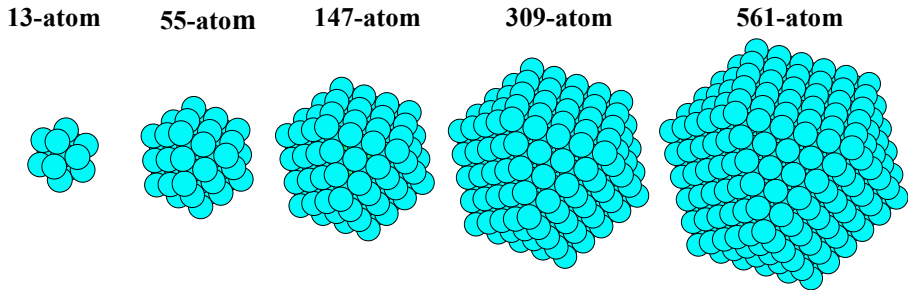

Figure 2.8. Magic-number cuboctahedral clusters obtained by surrounding an atom by successive shells of atoms of its kind. The magic numbers : 13, 55, 147, 309, 561 correspond to one-, two-, three-, four- and five-shell clusters, respectivily.

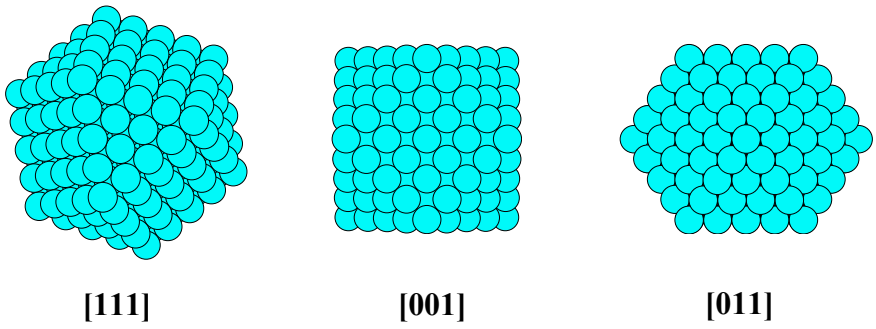

Figure 2.9. Schema of a 309-atom cuboctahedral Pt cluster imaged in three different zone axis directions : [111], [001] and [011].

In order to identify the most common cluster orientations, we obtained a map with several images of tilted nanocrystals (see in *figure*

2.10). The Pt nanocluster (in this case a platinum 309-atoms cluster) was tilted around the x-axis ([100]) from [001] to [010] zone axis in 5 º steps. We obtained the simulated images in the Scherzer defocus conditions (first contrast maximum). Microscope conditions were taken as 300 kV and C_s = 1.2 nm. The scale of the images changes in every sample. Image side lengths have a variation according to the calculated relation,

$$L = a(\cos a + sin a) \qquad (2.31)$$

where a is the unit constant (1.5680 nm) and a the tilt angle. Image length changes then with tilt angle, from 1.5680 nm for [001] and [010] zone axis (a = 0 and 90 º, respectively), to maximum of 2.2175 nm for [011] zone axis (a = 45 º). The simulations of a systematically tilted cuboctahedral metal cluster show images that appear to be like structural images even when the nanocluster is tilted several degrees away from bulk material zone axes. The apparent atomic structure in such images cannot be directly related to the real structure of the cluster [50].

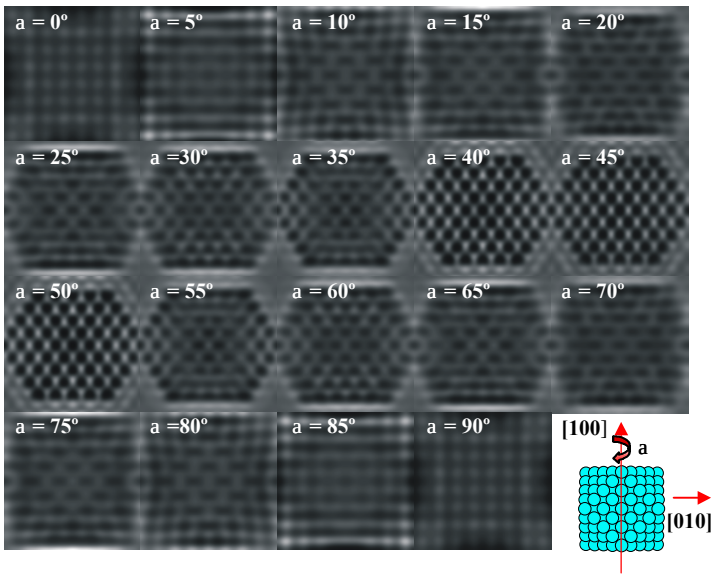

Figure 2.10. Map of simulated images for a 309-atom cuboctahedral Pt nanocluster in different tilts. The cluster was tilted around the x-axis ([100]) from [001] to [010] zone axis in 5 º steps. All images were obtained in the Scherzer defocus (first contrast maximum). Microscope conditions were taken as 300 kV and C_s = 1.2 nm. Notice that images are not in the same scale, image side lengths change with tilt angle, from 1.5680 nm for [001] and [010] zone axis(a = 0 and 90 º, respectively) , to 2.2175 nm for [011] zone axis (a = 45 º).

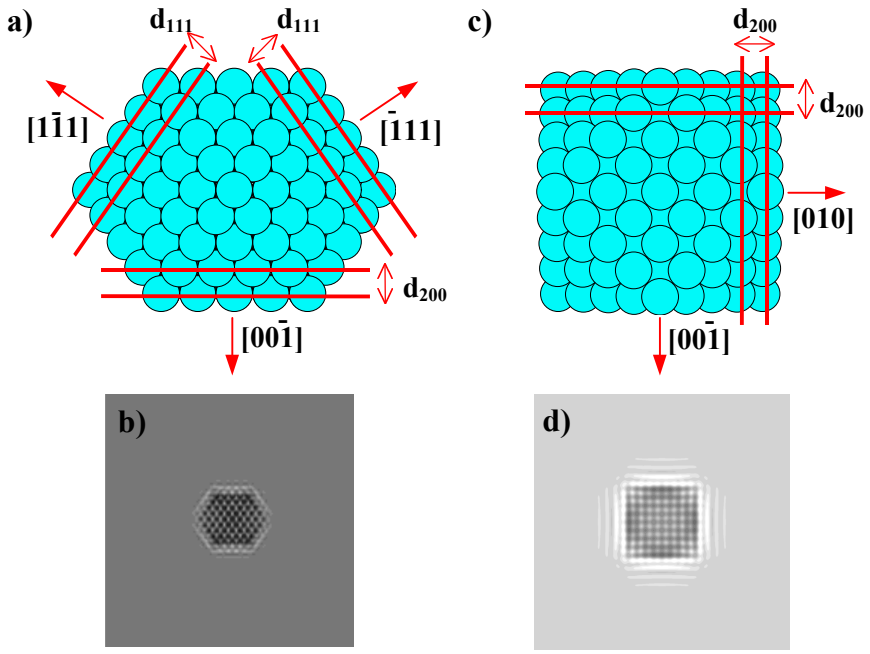

Figure 2.11. a) hard-sphere model of the cuboctahedron with regular triangular (111) facets, viewed down the [110] axis. The sets of low-index planes parallel to this axis are evidenced from their traces in the projection. d_{111} and d_{200} refer to the interplanar distances of {111}and {200} respectively. **b)** Simulated image of a cuboctahedron in the [110] orientation with 309 atoms in the crystal; side length of the image: 8.87 nm; sampling: 1024x1024 pixels; defocus: 45 nm (first maximum of contrast). **c)** Same cuboctahedron as in **a)**, but observed down [100]. **d)** Simulated of a cuboctahedron in the [100] orientation. 309 atoms in the crystal; side length of the image: 6.27 nm; sampling: 1024x1024 pixels; defocus 75 nm (second maximum of contrast).

In this way CIS is a useful tool to a priori determine the orientations that will give a good image resolution. In the images obtained in *figure 2.10*, we found that given the limited resolution in HRTEM images (1.9 Å point to point), in a fcc single crystal, only {111} (with 2.27 Å separation between planes) and {200} (with 1.96 Å) can be imaged. As a consequence, only two types of orientations lead to contrasts of atomic columns type: this appearance follows from the presence of more than one family of {111} or {200} planes parallel to the direction of observation [48]. The first is <110>, where two {111} and one {200} sets evidenced in *figure 2.11.a.* combine in

the image; the second is <100> where two {200} crossing at right angles are present [model in *figure 2.11 c)*]. Given our limited resolution, these orientations lead to the most informatory HREM images of the structure of a fcc crystallite. The same atomic column contrasts are also obtained in the simulated images of *figure 2.11 b)* and d) for the <110> and <100> orientations. For the <110> orientation, the calculated image is at the first maximum of contrast (black dots roughly correspond to the positions of the atomic columns) and for the <100> orientation image is at the second maximum of contrast (white dots now roughly correspond to the positions of atomic columns).

Complex Supercell Modelling and Simulation

The description made above corresponds to CIS of simple cluster morphologies. When we want to simulate a complex supercell including both, metal cluster and semiconductor support, a further study has to be made. In these complex systems, the first step consists in the evaluation of the orientation relationship between the metal cluster and support. DIP will provide us with the information about the zone axis and relative relation between the metal and oxide atomic planes involved in the experimental micrograph. Once we know the orientation and depending on the nature of the cluster imaged, we can follow two different ways:

a) If the metal cluster has been imaged in cross section, we are visualizing its profile. In this case, the orientation relationship can be directly associated with an epitaxial relation. The parallel planes placed on cluster and support interface correspond to the epitaxial planes, and the zone axis obtained gives the rotation over the epitaxy plane (see *figure 2.12.a*).
b) However, when the metal cluster is imaged in planar view, the orientation relationship can not be directly related with an epitaxial relation. As we show in *figures 2.12.b* and *2.12.c*, both supercell examples would show a similar TEM planar image in the zone axis selected. The main difference between both examples lies on the

epitaxial plane chosen. As a first approximation, we can always select the epitaxial plane as the perpendicular to the zone axis observed (*figure 2.12.c*). The main problem is that HRTEM images are obtained in 2D and do not provide information about the possible inclination of support surface. In this way, we will have to find all the possible metal and support epitaxial relations that are consistent with the orientation relationship found. The selection of a determinate epitaxial plane will determine the support inclination (*figure 2.12.d*). In order to select the most appropriate epitaxial planes, we can simulate the metal-oxide interface looking for the best atomic adaptation between cluster and support atoms (*figures 2.12.f* and *2.12.g*). In the examples presented, the best epitaxial relationship is obtained for the example presented in *figures 2.12. b,d,f.*

In order to complete our analysis, we can simulate the models selected in a map of HRTEM images obtained for different image defocus. The supercell model designed in *figure 2.12.a* has been simulated in *figure 2.13* with defocus values varying from –10 nm to –120 nm. After simulation we just need to compare the experimental images with the simulated and look for a good resemblance between them.

The complex supercell models used to carry out the CIS were built using the software *RHODIUS* [53] and *INDEM* [54].

In the case of *RHODIUS*, it was developed in Universidad de Cádiz, by the same group that implemented *EJEZ* and *RODAJAS*. This software application allows building in a flexible and controlled way the complex supercell models that we require for the interpretation of HRTEM images. This program contains several routines that allows the user to control the orientation of the crystals of the supported phase and the support inside the supercell, the size and shape of the supported phase, its position on the supports surface and the characteristics of the cluster/support interface [47].

In the case of *INDEM*, it was developed in CEMES-CNRS in Toulouse (France). This program allows the user to precisely build the supercell model of two epitaxed layers by using the orientation relationship

observed in HRTEM micrographs. In our case, platinum clusters acquire reduced sizes leading to small epitaxial interfaces. The use of programs like *INDEM* can be useful to simulate the interface of the biggest platinum clusters (lateral size > 5 nm), but it will not be so accurate for clusters with smaller sizes.

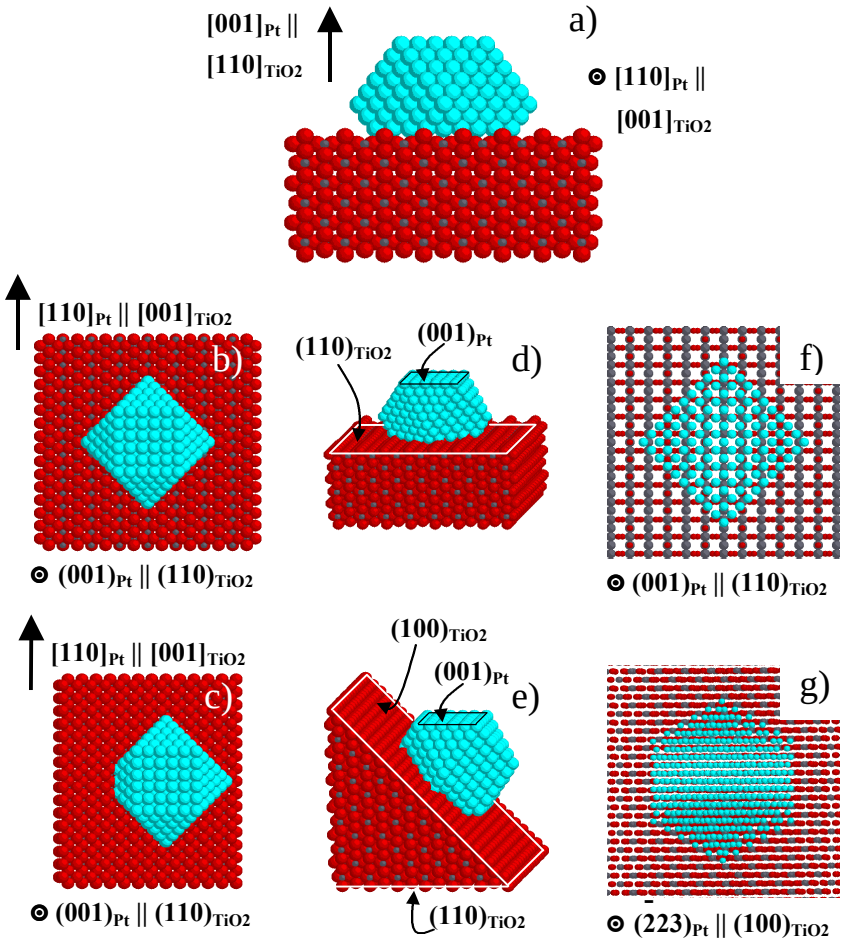

Figure 2.12. a) Supercell model in profile view. Two exemples of similar planar view models are shown in **(b)** and **(c)**. The diferences between both lie in the cluster/support epitaxial interface, **(d)** and **(e)** respectively. In **(f)** and **(g)** we show the simulated metal/semiconductor interface of epitaxy. Although both planar view examples could give quite similar HRTEM images, there is a big difference between both examples.

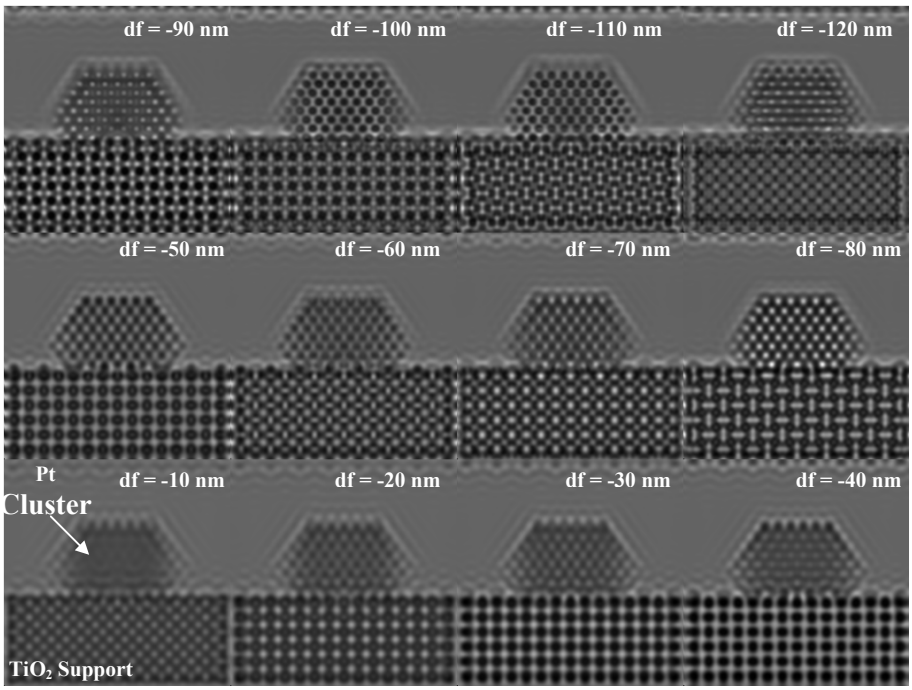

Figure 2.13. Map of simulated HRTEM images for the supercell model presented in *figure 2.12.a.* Images were obtained for different defocus values. Microscope conditions were taken as 300 kV and C_s = 1.2 nm. Image resolution is 256x256 pixels corresponding to 50x50 Å.

2.3.4 Selected Area Electron Diffraction

This technique basically consists in performing a diffraction pattern of a specified region of the sample. Diffraction patterns can be easily interpreted. We will obtain a set of spots, which corresponds to those families of planes that satisfy the Bragg's law in real space. These spots can be related to the distance between atomic material planes. After indexing our Selected Area Electron Diffraction (SAED) pattern, we will obtain useful information about the structural composition of our material.

If the specimen studied is polycrystalline (as it will be in our case), the random orientation of individual grains will create a set of concentric

rings in SAED pattern composed of fine spots. In *figure 2.14* we show an example of an indexed SAED pattern. To carry out this process we used a profile of SAED pattern image (*figure 2.14.b*) that has been properly scaled.

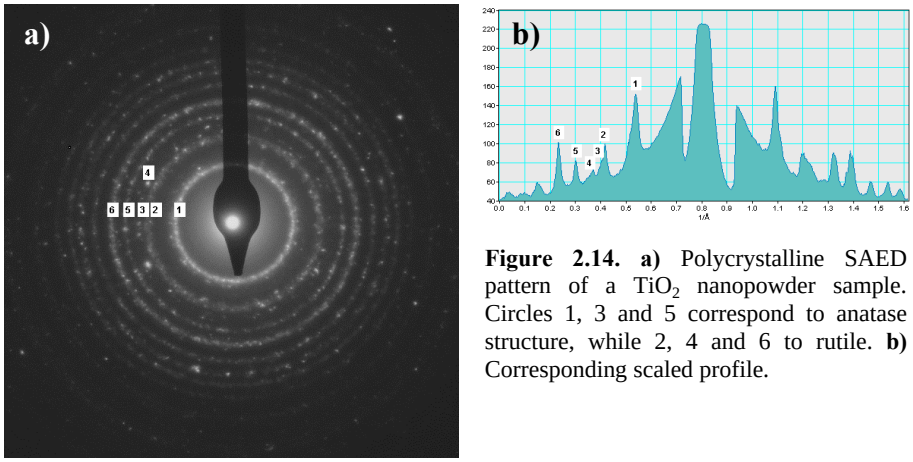

Figure 2.14. a) Polycrystalline SAED pattern of a TiO_2 nanopowder sample. Circles 1, 3 and 5 correspond to anatase structure, while 2, 4 and 6 to rutile. **b)** Corresponding scaled profile.

In *table 2.1* we show the results obtained after indexing. These results suggest a TiO_2 mixed anatase/rutile phase in our sample.

Ring	Distance (Å)	Atomic Plane	TiO_2 Phase
1	3.52	(101)	Anatase
2	2.49	(101)	Rutile
3	2.38	(004)	Anatase
4	2.19	(111)	Rutile
5	1.89	(200)	Anatase
6	1.69	(211)	Rutile

Table 2.1. Indexing results for SAED pattern shown in *figure 2.13*.

As commented before, spots obtained after FFT on a HRTEM digital image, can also be interpreted and indexed as SAED pattern spots. However, both techniques are space limited. It is difficult to obtain a SAED pattern of a single nanoparticle due to its reduced size and it is almost impossible to

obtain a HRTEM micrograph of few hundred nanograins at the same time. Moreover, in the case of powder polycrystalline catalysts, the identification of preferential orientations from electron diffraction patterns may require the use of a conventional selected area electron diffraction (SAED) technique with a narrow electron probe or even better nanodiffraction techniques [55]. Otherwise, many randomly oriented catalyst particles can contribute to the diffraction process, thus leading to ring patterns, with independence of the structural relationships existing between metal and support. In addition, the closeness of support and metal lattice spacings in the materials used, e.g. 2.19 and 2.30 Å for TiO_2 $\{1\bar{1}1\}$ and {200} respectively, and 2.27 Å for Pt {111} make difficult to resolve the diffraction spots due to platinum from those generated by the support lattice. These are the reasons why we selected SAED techniques in order to analyze the global material phases (*figure 2.14*), and FFT applied to HRTEM micrographs to study the particular morphology of a single metal cluster/support system.

2.3.5 Electron Dispersive X-ray Spectroscopy

Nowadays, modern electron microscopy can give resolutions of less than 2 Å, which is sufficient in order to characterize metallic cluster's morphology and its atomic structure. The applications of the HRTEM are actually increasing because of the possibility for combining it with other analytical methods. In this way, Energy Dispersive X-ray Spectroscopy (EDS) allows the identification of the elements, which form the cluster. We extensively used this technique to confirm results obtained from HRTEM micrographs. The main problem in the EDS used was the impossibility of detecting elements behind Na (Z=11). Elements such as B, C, N and O won't be detected. This is due to the use of a Be window to avoid contamination inside the microscope chamber, which only leads to detect elements below Na (Z=11). Thus, in the case of oxides we will just detect its metallic component. A typical EDS spectrum is shown in *figure 2.15*.

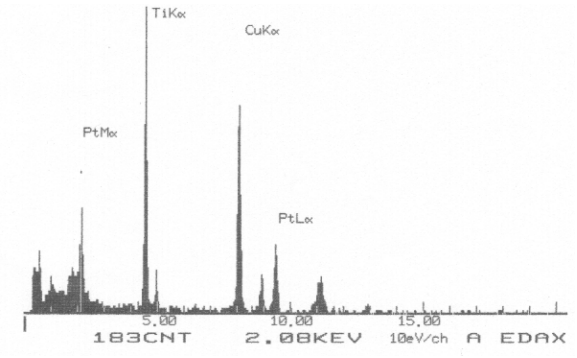

Figure 2.15. EDS spectrum of a sample containing Ti and Pt. The presence of Cu is due to the X-rays coming from the grid.

2.4 Equipment used for structural analysis

In the following, we will describe the main characteristics of the equipment used in this *Ph.D. Thesis work* for sample analysis.

2.4.1 Transmission Electron Microscopy

Philips CM30-SuperTwin - Serveis Científico-Tècnics UB (Barcelona) and CEMES-CNRS (Toulouse, France).

Electron Gun: LaB_6 — C_s = 1.2 mm
Acceleration Voltage: 300 kV — C_c = 1.2 mm
Magnification: Up to 700000x — Scherzer defocus = -56 nm
Structural Resolution: 0.19 nm
EDS analysis LINK LZ-5 with Si (Li) detector and window less.

JEOL 2000EX - Servicios Centrales de Ciencia y Tecnología UCA (Cádiz, Spain)

Electron Gun: LaB_6 — C_s = 0.7 mm
Acceleration Voltage: 200 kV — C_c = 1.2 mm
Magnification: Up to 600000x — Scherzer defocus = -51 nm
Structural Resolution: 0.21 nm

2.4.2 Digital Image Processing

SOFTWARE

Digital Micrograph (Gatan)
FFT and filters related
SAED pattern indexing
Image calibration

Photoshop 5.0 (Adobe)
General Image Processing

Filter (homemade)
Convolution Filters
Median Filter

EJEZ (University of Cádiz)
Establishment of materials zone axis [53].

2.4.3 Computer Image Simulation

Carine Crystallography 3.1 (DIVERGENT)
Creation of materials cells
Metal Supercells
Zone axis
XRD patterns

RHODIUS (Universidad de Cádiz)
Complex Supercell files creation [53].

RODAJAS (Universidad de Cádiz)
Supercell files division in thin slices.

EMS (University of Lausanne)
Computer Simulated HRTEM images [42, 43, 44, 45]

INDEM (CEMES-CNRS)
Supercells of epitaxial materials [54].

2.4.4 General Analytical Techniques Applied

2.4.4.1 XRD Spectroscopy

X-ray powder diffractometer SIEMENS D-500
X-ray generator: Kristalloflex 710H
Scintillator detector
Graphite Secondary monochromator
Cu tube

2.4.4.2 Raman Spectroscopy

Jobin-Ybon T64000 spectrometer

Coupled to an *Olympus metallographic microscope*.
Excitation wavelength: 514.5 nm (argon-ion laser)
Incident Power: 2 mW.

2.4.4.3 ICP Spectroscopy

Perkin-Elmer Optima 3200 RL spectrometer
Measurements carried out: Induced Coupled Plasma-Optical Emission Spectroscopy (ICP-OES) measurements.
Radiofrequency source: 40MHz
Working power: between 750 and 1500 W
SCD detector with simultaneous measure of 235 subarrays

In the following *Chapters*, we will apply the techniques described above to the analysis of the nanoscopic characteristics of the metal additive distribution in semiconductor gas sensor materials. In this way, *Metal Diffusion*, *Superficial Metal Clustering*, *Metal Macro-Agglomeration* and *Metal Ultradispersion* will be widely studied taking in every case the material system examples most commonly used in SGS field.

References

1. G. Cerrato, L. Marchese and C. Morterra, Structural and morphological modifications of sintering microcrystalline TiO_2: an XRD, HRTEM and FTIR study, *Applied Surface Science*, **70/71**, 200-205 (1993).

2. A. Ueda, T. Nakao, M. Azuma and T. Kobayashi, Two conversion maxima at 373 and 573 K in the reduction of nitrogen monoxide with hydrogen over Pd/TiO_2 catalyst, *Catalysis Today*, **45**, 135-138 (1998).

3. A. Turkoviæ, M. Ivanda, S. Popoviæ, A. Tonejc, M. Gotiæ, P. Dubèek and S. Musiæ, Comparative Raman, XRD, HREM and SAXS studies of grain sizes in nanophase TiO_2, *Journal of Molecular Structure*, **410-411**, 271-273 (1997).

4. L.E. Depero, L. Sangaletti, B. Allieri, E. Bontempi, R. Salari, M. Zocchi, C. Casale, M. Notaro, Niobium-titanium oxide powders obtained by laser-laser induced synthesis: Microstructure and structure evolution from diffraction data, *Journal of Materials Researh*, **13 (6)**, 1644-1649 (1998).

5. H. P. Klug, L. E. Alexander, X-ray diffraction procedures, *John Wiley and Sons Inc.*, New York (1954).

6. B. E. Warren, X-ray diffraction, *Dover publications, Inc.,* New York (1990).

7. F. Plana, La difracció de raigs X com a eina de caracterització de materials ceràmics, *Butlletí de la Societat Catalana de Ciència*, XIII, 449-461 (1992).

8. J.- M. Pan, B. L. Maschhoff, U. Diebold and T. E. Madey, Structural study of ultrathin metal films on TiO_2 using LEED, ARXPS and MEED, *Surface Science*, **291**, 381-394 (1993).

9. A. R. Phani, S. Manorama and V. J. Rao, The nature of surface behavior of tin oxide doped sensors: X-ray photoelectron spectroscopy studies before and after exposure to liquid petroleum gas, *Journal of Physics and Chemistry of Solids*, **61**, 985-993 (2000).

10. R. Rella, P. Siciliano, S. Capone, M. Epifani, L. Vasanelli and A. Licciuli, Air quality monitoring by means of sol-gel integrated tin oxide thin films, *Sensors and Actuators B*, **58**, 283-288 (1999).

11. M.Z. Atashbar, H.T. Sun, B. Gong, W. Wlodarski, R. Lamb, XPS study of Nb-doped oxygen sensing TiO_2 thin films prepared by sol-gel method, *Thin Solid Films*, **326**, 238-244 (1998).

12. A. Cabot, J. Arbiol, J. R. Morante, U. Weimar, N. Bârsan and W. Göpel, Analysis of the noble metal catalytic additives introduced by impregnation of as obtained SnO_2 sol-gel nanocrystals for gas sensors, *Sensors and Actuators B*, **70**, 87-100 (2000).

13. J. F. Moulder, W. F. Stickle, P. E. Sobol, K. D. Bomben, Handbook of X-ray Photoelectron Spectroscopy, *J. Chastain, ed., Perkin-Elmer Corp.,* Minnesota (1979).

14. D. Briggs and M. P. Seah, Practical Surface Analysis vol. 1: Auger and X-ray Photoelectron Spectroscopy, *John Wiley and Sons.*, Chichester (1990).

15. G. A. Tompsett, G. A. Bowmaker, R. P. Cooney, J. B. Metson, K. A . Rodgers and J. M. Seakins, The Raman Spectrum of Brookite, TiO_2 (Pbca, Z = 8), *Journal of Raman Spectroscopy*, **26**, 57-62 (1995).

16. R. J. González, Raman, Infrared, X-ray, and EELS Studies of Nanophase Titania, *Ph. D. Thesis*, Blacksburg, Virginia (USA), (1996).

17. A. Cabot, A. Diéguez, A. Romano-Rodríguez, J. R. Morante and N. Bârsan, Influence of the catalytic introduction procedure on the nano-SnO_2 gas sensor performances. Where and how stay the catalytic atoms?, *In press Sensors and Actuators B*.

18. K. Nakamoto, Infrared and Raman Spectra of Inorganic and Coordination Compounds, *John Wiley and Sons Inc.*, New York (1986).

19. J. G. Grasselli and B. J. Bulkin, Analytical Raman Spectroscopy, *John Wiley and Sons Inc.,* New York (1991).

20. http://www.tjasolutions.com/instruments/icpoes/product_icp_oes.asp

21. http://www.tjasolutions.com/instruments/icpoes/fundamental_icp.asp

22. R. Díaz, J. Arbiol, A. Cirera, F. Sanz, F. Peiró, A. Cornet and J. R. Morante Electroless Addition of Catalytic Pd to SnO_2 Nanopowders, submitted to *Chem. Mat.*

23. R. Díaz, J. Arbiol, A. Cirera, F. Sanz, F. Peiró, A. Cornet and J. R. Morante, Electroless Addition of Catalytic Pt to SnO_2 Nanopowders, submitted to *J. Mat. Chem.*

24. http://www.sct.ub.es/serveis/01030204/uhom_000.htm

25. D. B. Williams and C. B. Carter (Ed.), Transmission Electron Microscopy: a Textbook for Materials Science, *Plenum Press*, New York (1996).
26. G. Schmid (Ed.), Clusters and Colloids: From Theory to Applications, *VCH*, Venheim (1994).
27. C. Bonafos, B. Garrido, M. Lopez, A. Perez-Rodriguez, J. R. Morante, Y. Khin, G. Ben Assayag and A. Claverie, An electron microscopy study of the growth of Ge nanoparticles in SiO_2, *Applied Physics Letters*, **76 (26)**, 3962-3964 (2000).
28. P. J. Grundy and G. A. Jones, Electron Microscopy in the Study of Materials, B. R. Coles and E. Arnold (Ed.), London (1976).
29. A. Diéguez, Structural Analysis for the improvement of SnO_2-Based Gas Sensors, *PhD. Thesis*, Universitat de Barcelona, Barcelona (1999).
30. O. Dulub, W. Hebenstreit and U. Diebold, Imaging Cluster Surfaces with Atomic Resolution: The Strong Metal-Support Interaction State of Pt Supported on TiO_2(110), *Physical Review Letters*, **84 (16)**, 3646-3649 (2000).
31. S. Bernal, F. J. Botana, J. J. Calvino, C. López, J. A. Pérez-Omil and J. M. Rodríguez-Izquierdo, High-resolution electron microscopy investigation of metal-support interactions in Rh/TiO_2, *Journal of the Chemical Society, Faraday Trans.*, **92 (15)**, 2799-2809 (1996).
32. S. Bernal, J. J. Calvino, M. A. Cauqui, J. A. Pérez Omil, J. M. Pintado and J. M. Rodríguez-Izquierdo, Image simulation and experimental HREM study of the metal dispersion in Rh/CeO_2 catalysts. Influence of the reduction/reoxidation conditions, *Applied Catalysis B: Environmental*, **16**, 127-138 (1998).
33. M. José-Yacamán, G. Díaz and A. Gómez, Electron Microscopy of catalysts; the present, the future and the hopes, *Catalysis Today*, **23**, 161-199 (1995).
34. S. Bernal, F. J. Botana, J. J. Calvino, G. A. Gifredo, J. A. Pérez Omil and J. M. Pintado, HREM study of the behavior of a Rh/CeO_2 catalyst under high temperature reducing and oxidizing conditions, *Catalysis Today*, **23**, 219-250 (1995).
35. S. Bernal, J. J. Calvino, M. A. Cauqui, J. A. Pérez Omil, J. M. Pintado and J. M. Rodríguez-Izquierdo, Image simulation and experimental HREM study of the metal dispersion in Rh/CeO_2 catalysts. Influence of the reduction/reoxidation conditions, *Applied Catalysis B: Environmental*, **16**, 127-138 (1998).
36. A. Alimoussa, M.- J. Casanove and J. L. Hutchison, Transmission electron microscopy and high-resolution electron microscopy of growth defects in $La_{2-x}Sr_xCuO_4$ thin films, *Philosophical Magazine A*, **76 (5)**, 907-919 (1997).

37. M. P. Ekstrom, Digital Image Processing Techniques, *Academic Press* (Ed.), Orlando (1984).
38. A. Domingo Asenjo, Tratamiento Digital de Imágenes, *Anaya Multimedia* (Ed.), Madrid (1993).
39. W. H. Press, Numerical recipes in C: the art of scientific computing, *Cambridge University Press* (Ed.), Cambridge (1992).
40. A. Mata, Turbo C / C++ iniciación y programación avanzada, *Paraninfo* (Ed.), Madrid (1995).
41. M. A. O'Keefe, P. R. Buseck and S. Iijima, Computed crystal structure images for high resolution electron microscopy, *Nature*, **274**, 322-324 (1978).
42. P. A. Stadelmann, EMS – A Software Package for Electron Diffraction Analysis and HREM Image simulation in Material Science, *Ultramicroscopy*, **21**, 131-146 (1987).
43. P. A. Stadelmann and P.A. Buffat, Simulation of High Resolution Electron Microscope Images and 2-dimensional Convergent Beam Electron Diffraction Patterns, *Computer Simulation of Electron Microscope Diffraction and Images*, Ed. W. Krakow and M. O'Keefe, *The Minerals, Metals & Materials Society*, (1989).
44. P. A. Stadelmann (Ed.), EMS User's Guide, Lausanne, (1993).
45. P. A. Stadelmann, EMS – A software package for electron diffraction analysis and HREM image simulation in materials science, *Ultramicroscopy*, **56**, 11-25 (1994).
46. S. Bernal, F. J. Botana, J. J. Calvino, G. A. Gifredo, J. A. Pérez Omil and J. M. Pintado, HREM study of the behavior of a Rh/CeO_2 catalyst under high temperature reducing and oxidizing conditions, *Catalysis Today*, **23**, 219-250 (1995).
47. C. López-Cartes, Aspectos Nanoestructurales de los Fenómenos de Interacción Metal-Soporte en los Catalizadores Modelo Metal/Óxido de Cerio, *PhD. Thesis*, Universidad de Cádiz, (2000).
48. P.- A. Buffat, M. Flüeli, R. Sopycher, P. Stadelmenn and J.- P. Borel, Crystallographic Structure of Small Gold Particles studied by High-resolution Electron Microscopy, *Faraday Discussions*, **92**, 173-187 (1991).
49. Y. Volokitin, J. Sinzig, L. J. de Jongh, G. Schmid, M. N. Vargaftik and I. I. Moiseev, Quantum-size effects in the thermodynamic properties of metallic nanoparticles, *Nature*, **384**, 621-623 (1996).
50. J.- O. Malm and M. A. O'keefe, Deceptive "lattice spacings" in high-resolution micrographs of metal nanoparticles, *Ultramicroscopy*, **68**, 13-23 (1997).

51. M.- J. Casanove, P. Lecante, E. Snoeck, A. Mosset and C. Roucau, HREM and WAXS Study of the Structure of Metallic Nanoparticles, *Journal of Physics III France*, **7**, 505-515 (1997).

52. http://www.thuntek.net/~jwills/GIG/C/Cuboctahedral_packing.html

53. J.A. Pérez-Omil, Interpretación sistemática de Imágenes de Microscopía Electrónica de Alta Resolución de Materiales Policristalinos. Estudio de Catalizadores Metálicos soportados, *PhD. Thesis*, Universidad de Cádiz, (1994).

54. J. Arbiol, A. Ruiz, A. Cirera, F. Peiró, A. Cornet, J. R. Morante, A. Alimoussa and M.- J. Casanove, High Resolution Electron Microscopy analysis of Pt-nanoparticles embedded on crystalline TiO_2, to be published in *Inst. Phys. Conf. Ser*.

55. S. Bernal, F. J. Botana, J. J. Calvino, C. López, J. A. Pérez-Omil and J. M. Rodríguez-Izquierdo, High-resolution electron microscopy investigation of metal-support interactions in Rh/TiO_2, *Journal of the Chemical Society, Faraday Trans.*, **92(15)**, 2799-2809 (1996).